Near-Source Waveform Modeling to Estimate Shallow Crustal Attenuation and Radiated Energy of M_w 2.0–4.5 Earthquakes

Keisuke Yoshida[1], Kentaro Emoto[2], Shunsuke Takemura[3], Toru Matsuzawa[1]

1: Research Center for Prediction of Earthquakes and Volcanic Eruptions, Graduate School of Science, Tohoku University, Sendai, Japan
2: Institute of Seismology and Volcanology, Kyushu University, Fukuoka, Japan
3: Earthquake Research Institute, The University of Tokyo, Tokyo, Japan

Corresponding author: Keisuke Yoshida, Research Center for Prediction of Earthquakes and Volcanic Eruptions, Tohoku University, 6-6 Aza-Aoba, Aramaki, Aoba-Ku, Sendai, 980-8578, Japan (keisuke.yoshida.d7@tohoku.ac.jp)

Key Points (<140 characters)

1. We estimated the shallow Q-structure using high-quality near-source (< 12 km) seismic data by matching observed and synthetic waveforms.
2. The shallow (< 4 km) crust has a low Q_s-value (~55), influencing the estimation of the moment-scaled radiated energy (e_R) of small events.
3. The e_R of 3,884 M_w 2.0–4.5 events based on the refined Q-model has a median value of 3.6×10^{-5} and does not show an obvious scale dependence.

Abstract (242 ≤ 250 words)

Estimating the radiated energy of small-to-moderate (M_w < 5) events remains challenging because their waveforms are strongly distorted during wave propagation. Even when near-source records are available, seismic waves pass through the shallow crust with strong attenuation; consequently, high-frequency energy may be significantly dissipated. Here, we evaluated the degree of energy dissipation in the shallow crust by estimating the depth-dependent attenuation (Q^{-1}) by modeling near-source (< 12 km) waveform data in northern Ibaraki Prefecture, Japan. High-quality waveforms recorded by a downhole sensor confined by granite with high seismic velocity helped to investigate this issue. We first estimated the moment tensors for M1–4 events and computed their synthetic waveforms, assuming a tentative one-dimensional Q^{-1}-model. We then modified the Q^{-1}-model in the 5–20 Hz range such that the frequency components of the synthetic and observed waveforms of small events (M_w < 1.7) matched. The results show that the Q_s-value is 55 at depths of < 4 km and shows no obvious frequency dependence. Using the derived Q^{-1}-model, we estimated the moment-scaled energy (e_R) of 3,884 events with M_w 2.0–4.5. The median e_R is 3.6×10^{-5}, similar to the values reported for M_w >6 events, with no obvious M_w dependence. If we use an empirically derived Q_s-model (~350), the median e_R becomes a one-order underestimation (3.1×10^{-6}). These results indicate the importance of accurately assuming the Q-value in the shallow crust for energy estimation of small events, even when near-source high-quality waveforms are available.

Plain language summary (199 ≤ 200 words)

A good understanding of the energy-radiation characteristics of small earthquakes is the basis for understanding the differences in the generation processes between small and large events. However, estimating the radiated energy for small (M_w<5) events is still challenging because their waveforms are significantly distorted during wave propagation. To evaluate the degree of energy dissipation in the shallow crust, we used high-quality near-source (< 12 km) waveform records from northern Ibaraki Prefecture, Japan. We estimated the attenuation structure by matching the synthetic and observed spectral amplitudes in multiple frequency bands. The results show that energy dissipation is fairly large in the shallow (< 4 km) part. We used the derived attenuation structure to estimate the moment-scaled energy (e_R) of 3,884 small events (M_w 2.0–4.5). The median value was 3.6×10^{-5}, which is similar to the values reported for larger (M_w > 6) events, with no obvious difference in magnitude. If we assume a standard attenuation value, the e_R erroneously becomes too small (median of 3.1×10^{-6}), requiring a significant increasing trend with magnitude. These results indicate the importance of accurately determining the attenuation of the shallow crust to estimate the energy radiation of small events, even when near-source records are available.

1. Introduction

The precise quantification of energy radiation from small earthquakes provides a basis for understanding the differences and similarities between the physical processes of small and large earthquakes. The most straightforward approach to estimating the radiated energy (E_R) of an earthquake is to analyze seismic waveform records obtained at good near-source stations, where wave propagation effects can be negligible (Abercrombie, 1995; Kanamori et al., 1993 and 2020). Kanamori et al. (2020) recently employed this type of method to systematically estimate E_R for 29 $M_w > 5.6$ events in the crust of Japan. However, estimating E_R for small ($M_w < 5$) events is generally more difficult than for large events ($M_w > 6$). This is because high-frequency (f > 5 Hz) radiated energy, which is significantly dissipated during wave propagation, is critical for evaluating small events.

The energy dissipation during wave propagation is described by the inverse of the seismic quality factor, $Q^{-1} = -\frac{\Delta E}{2\pi E}$, where E is the energy of a seismic wave, and ΔE is the energy lost during one cycle. Assuming $Q^{-1} \ll 1$, amplitude attenuation over elapsed time t is related to Q^{-1} as follows:

$$\ln\big(A(f)\big) = -\pi f Q^{-1}(f) t - \gamma \ln(r) + \ln C(f), \quad (1)$$

where f is frequency; $A(f)$ is the spectral amplitude of P- or S-waves at a certain station; r is the wave-propagation distance; γ is the exponent of the geometric spreading factor depending on the ray path; and $C(f)$ includes the source- and site-effects on amplitude. Here, Q^{-1} is a combination of amplitude attenuation owing to intrinsic absorption and scattering losses (summarized in Sato et al., 2012). If Q-value is constant, the attenuation (the first term on the right-hand side of Eq. 1) increases exponentially as f or t increases. To avoid losing high-frequency information, it is essential to use records with a small t (i.e., a small distance).

A severe problem in examining small events is the possible strong attenuation (high Q^{-1}, i.e., low Q) of seismic waves in the shallow part of the crust (Anderson & Hough, 1984; Hauksson et al., 1987; Aster & Shearer, 1991). If the Q-value of the shallow crustal is very small, near-source observations can miss substantial high-frequency energy, which is important for estimating the source parameters of

small events (Frankel, 1982; Anderson, 1986; Abercrombie, 1997, 2000; Ide et al., 2003). Abercrombie (1997) suggested that even granite rocks have a very small Q (<50) at shallow depths (< 3 km), which influences high-frequency waveforms. Such a strong shallow attenuation was sometimes empirically estimated as a site effect, represented by parameters such as κ (Anderson & Hough, 1984; Oth et al., 2011; Edwards et al., 2015; Hassani & Atkinson, 2018; Haendel et al., 2023) or $f_{\max}$ (Hanks, 1982). However, obtaining the depth profile of the Q^{-1}-structure is essential for adequately understanding this effect. Previous studies have estimated Q-values that vary with depth (Hough & Anderson, 1988; Lin and Jordan, 2018; Wang et al., 2023), horizontally (Eulenfeld & Wegler, 2017; Prudencio et al., 2018), and in three dimensions (Eberhart-Phillips, 2005; Hauksson & Shearer, 2006; Nakajima & Matsuzawa, 2017; Nakamura & Shiina, 2019), with various assumptions. However, few studies have examined the depth variation of the Q^{-1}-structure within the crust in detail given that most available data are far from the sources (>15 km).

The National Research Institute for Earth Science and Disaster Resilience (NIED) Hi-net operates an excellent borehole seismic station (N.JUOH) in northern Ibaraki Prefecture, Japan, which helps to investigate this issue. Site effects usually include both site amplification and shallow attenuation, which makes them difficult to separate. However, the downhole sensor of this station is confined by granite rock with high velocity (Vp=5.4 km/s, Vs=3.2 km/s, and a depth of 100 m (https://www.kyoshin.bosai.go.jp/cgi-bin/kyoshin/db/siteimage.cgi?0+/IBRH14+kik+pdf), and the site amplification effect can be well taken into account. Intense seismicity has occurred in this region since the 2011 M9 Tohoku earthquake (Fig. 1; Yoshida et al., 2019a), and this downhole sensor records many earthquake waveforms within ten kilometers. Recently, Yoshida (2023) showed that the waveforms recorded at this sensor are clean enough to directly examine the moment-rate function for M_{w} >3.3 events from the P-wave shapes.

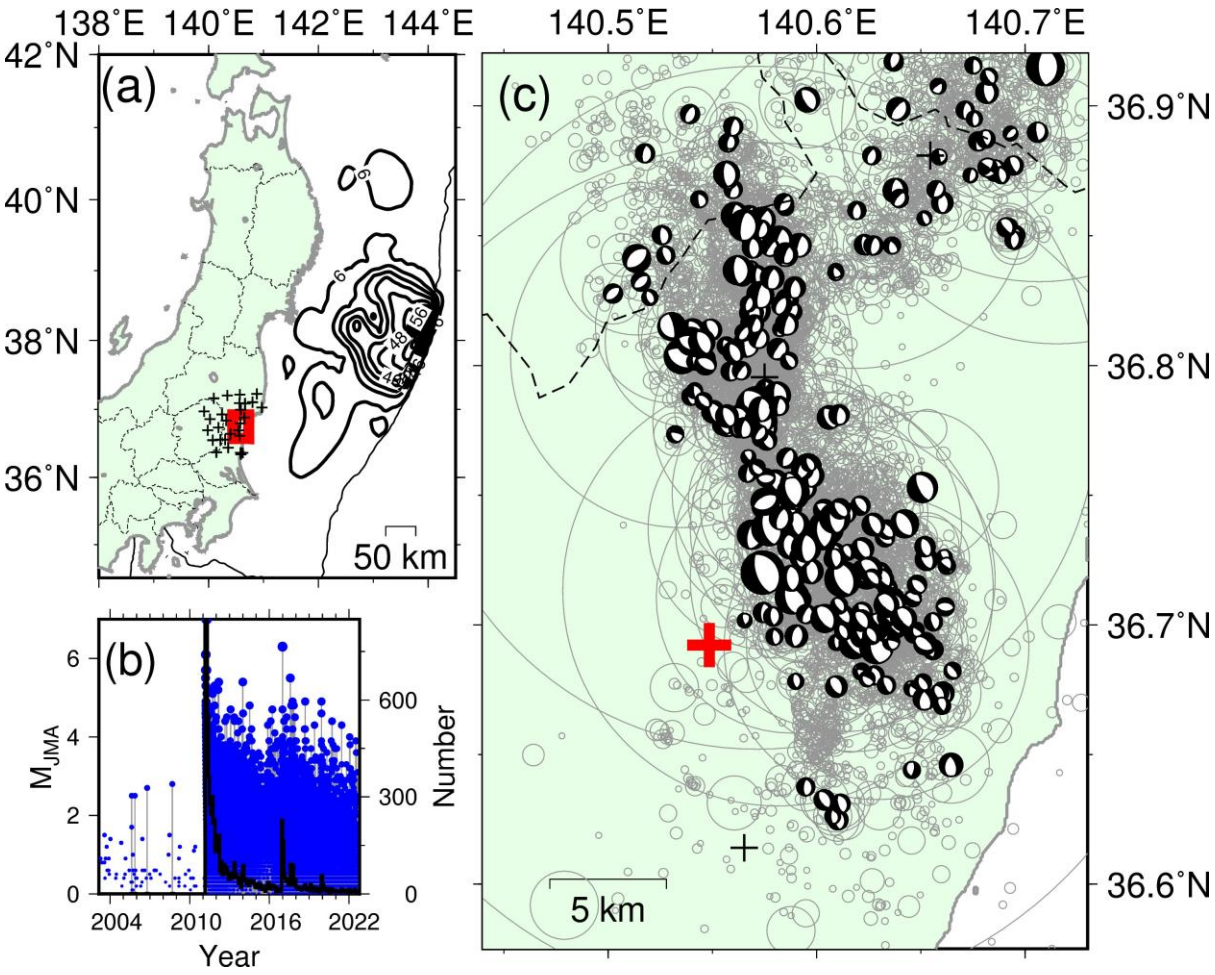

Figure 1. (a) Map showing the location of the study region represented by a red rectangle. The black contour lines show the coseismic slip distribution of the 2011 M9 Tohoku earthquake by Iinuma et al. (2012). Crosses indicate the seismic stations used for hypocenter relocation. (b) Magnitude–time diagrams of events in the study region. Blue circles with gray bars indicate the earthquake magnitudes in the Japan Meteorological Agency (JMA) unified catalog. The black line denotes the number of earthquakes with an amplitude-based magnitude reported by the JMA ($M_{\mathrm{JMA}} \geq 2.0$). (c) The study region. The red cross denotes the station (N. JUOH) whose waveforms are analyzed in this study. Gray circles show the hypocenters of shallow earthquakes (z < 40 km) with an $M_{\mathrm{JMA}} \geq 2.0$ from January 1, 2003, to September 30, 2022. The circle sizes correspond to the diameters of Eshelby's (1957) circular fault with a stress drop of 3 MPa. Beach balls show the moment tensor solutions by the F-net catalog.

139 The use of clean waveforms at near-source (< 12 km) distances helps examine
140 shallow attenuation in detail because propagation path effects generally accumulate
141 with increasing distance, and multipath effects appear at distant stations. In this study,
142 we used the high-frequency waveforms (5–20 Hz) recorded by this sensor to estimate
143 the Q-structure in the shallow crust. In estimating Q-value, many previous studies used
144 various assumptions, such as the ω^2-model (Brune, 1970), negligible effects of rupture
145 directivity, and spatially uniform and/or frequency-independent Q-condition. However,
146 we did not use such assumptions, taking advantage of the sufficient signal-to-noise
147 ratios of small ($M_w \leq 1.7$) events. We modeled the propagation effect using synthetic
148 waveforms based on one-dimensional (1-D) structures of Q-value, seismic velocity,
149 and density. The use of synthetic waveforms can naturally incorporate the effects of
150 near-field and intermediate terms, geometrical spreading, impedance contrast, and
151 surface reflections above the downhole sensor. Based on the estimated Q^{-1}-model, we
152 systematically estimate the e_R for small (M_w 2.0–4.5) events.
153 Subsequent sections are organized as follows. We estimate the 1-D velocity
154 model and moment tensor solutions of small events (Subsection 2) to compute synthetic
155 waveforms. We then compare the observed waveforms for small ($M_w \leq 1.7$) events with
156 the synthetic waveforms (Section 3). This comparison allowed the estimation of the
157 depth-dependent Q^{-1}-structure. Finally, we use the obtained depth-dependent
158 Q^{-1}-structure to estimate the radiated energies of small events (Section 4).
159
160 **2. Estimation of input parameters for synthetic waveform computation**
161 We retrieved information to compute the synthetic waveforms of small events for
162 comparison with the observed waveforms. We first estimate the 1-D velocity structure
163 and earthquake hypocenters (Subsection 2.1). We also derived the moment tensors for
164 events that were sufficiently small to avoid the finiteness effect on seismic waveforms
165 in the frequency band of interest (< 20 Hz) (Subsection 2.2). The waveform of an
166 earthquake is affected not only by path and site effects but also by the rupture process.
167 Often, corrections are made using the ω^2-model (Aki, 1967; Brune, 1970), but it has
168 become clear in recent years that complex events deviating from the ω^2-model are not

uncommon even for small events (Uchide & Imanishi, 2016; Pennington et al., 2023; Yoshida & Kanamori, 2023). Thus, we used the waveforms of very small events to avoid the influence of their source processes in the used frequency band.

2.1. Hypocenters and depth-dependent velocity structure

Here, we refine the 1-D velocity model for detailed comparisons between the synthetic and observed waveforms. The joint determination method of Kissling et al. (1994) was used to determine the 1-D velocity model and earthquake hypocenters. Both for the 1-D velocity structure estimation and hypocenter relocation, the data were the arrival times of the P- and S-waves of events derived from the JMA-unified catalog. Figure 1(a) shows the station distribution; we included data within 30 km of the epicenter.

We first use 1,256 $M_{\mathrm{JMA}} \geq 3$ events to estimate 1-D seismic velocities and station corrections. We adopted the hypocenters listed in the JMA-unified catalog as the initial locations. For the initial velocity model, we adopted the model proposed by Hasegawa et al. (1978) that was used for routine processing at Tohoku University (broken line in Fig. 2b). The JMA2001 model (Ueno et al., 2002) was also tested as the initial velocity model. However, this model exhibits an abrupt velocity change at a depth of 3 km. This change in velocity generated reflected waves that did not appear in the observed waveforms. Therefore, we chose the model of Hasegawa et al. (1978) because it has no abrupt velocity changes in the shallow part. We added a low-velocity layer at depths < 10 m, according to that reported by the NIED. The depth variation in seismic velocity was approximated using 16 layers.

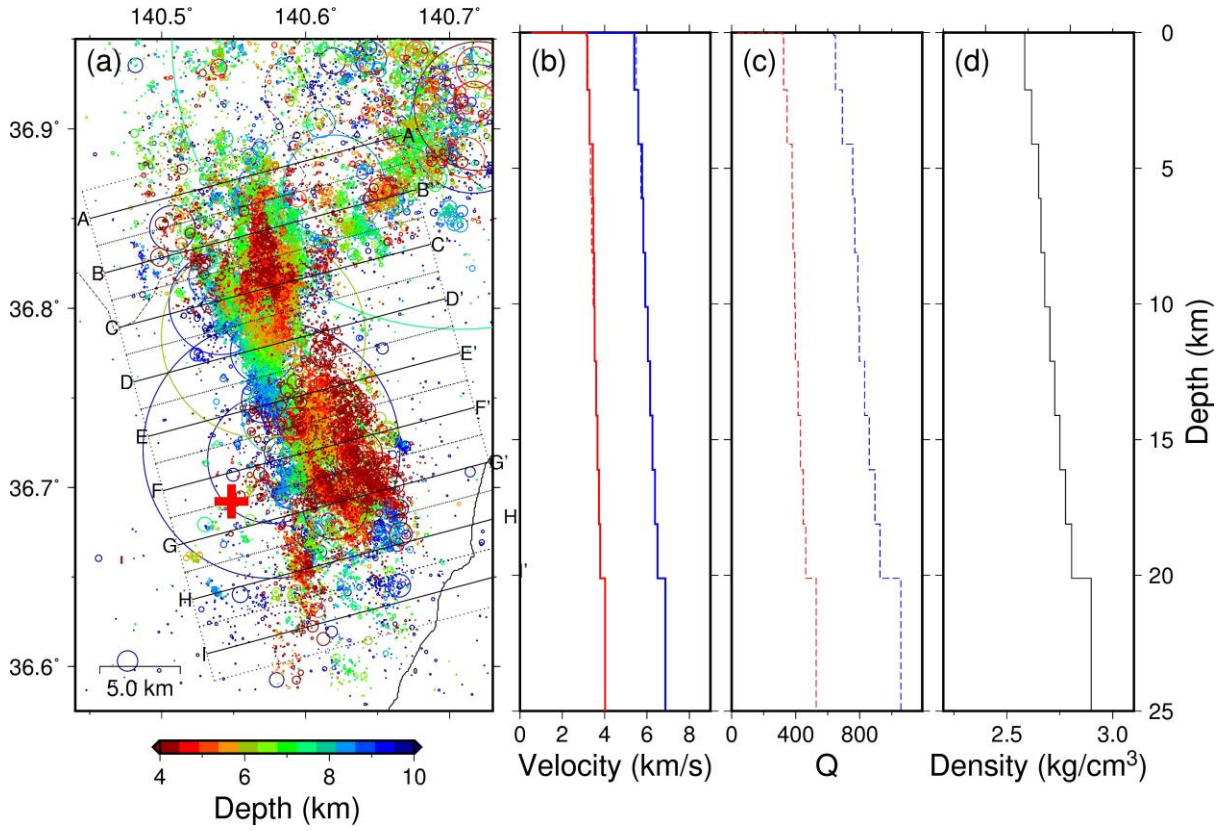

Figure 2. Epicenter distribution and the one-dimensional (1-D) models of seismic velocity, Q-value and density. (a): Epicenter distribution. The size of the circle represents the diameter of the circular fault in Eshelby (1957), assuming a stress drop of 3 MPa. The lines from A to I represent the locations of the cross sections in Fig. S1. (b), (c), and (d): 1-D models of seismic velocity, Q-value, and density, respectively. The broken line in (b) shows the initial model.

We set station N.JUOH (red cross in Fig. 1c and 2a), which is closest to the epicenters and has a high seismic velocity at the sensor depth, as the reference station for which the station correction of the P-wave arrival time is assumed to be zero. The velocity structure obtained is shown in Fig. 2(b). The obtained model is similar to the initial model. However, the change in velocity structure and the introduction of the station corrections reduced the mean arrival time residual from 0.10 s to 0.057 s. The station corrections obtained are shown in Table S1, where the correction value for the S-wave at N. JUOH was 0.01 s.

Using the obtained velocity model and station corrections, we relocate the hypocenters of 35,336 events with $M_{JMA} \geq 1$ in the JMA catalog. Figure 2(a) and S1 show the relocated hypocenters. The mean standard errors of the hypocenters are 0.19 km, 0.12 km, and 0.24 km in longitude, latitude, and depth, respectively. Even though we did not use the relative relocation method based on precise waveform correlation data, we obtained a detailed fault structure (Fig. S1) owing to the stations directly above the earthquakes.

2.2. Moment tensors of M_{JMA} 1–4 events

We determined the moment tensors for events whose source durations were sufficiently small to be negligible in the frequency band of interest (< 20 Hz). The source corner frequency of an M_w 1.7 event is approximately 32 Hz, according to Brune's (1970) source model, with a typical stress parameter of 3 MPa in the crust of Japan (Yoshida & Kanamori, 2023) and a focal depth of 10 km. Thus, we attempt to estimate the moment tensors for events with M_w 1.7 or less.

We estimated the moment tensors of small events from March 2003 to July 2022 using the amplitudes of direct P- and S-waves. To avoid path and site effects, we corrected the amplitudes using those of a reference event with a known focal mechanism. We used the procedure of Yoshida et al. (2019b), which follows Dahm (1996), and utilized the amplitude ratios of the waveforms among different events.

Figure 1(a) shows the distribution of the seismic stations used. Our data represent the amplitude ratios of the P, SH, and SV waves of each target event to those of the reference events. By limiting the distance between the target and reference events to less than 3 km, we first computed the cross-correlation coefficient of each phase between each pair of target and reference events. If the coefficient was > 0.8, the amplitude ratio was derived. If amplitude ratio data were obtained from more than eight stations, the moment tensor of the target event was determined by solving the linear equation of Dahm (1996). When there were multiple reference events for each target event, we used the amplitude ratio data from all events. We compute 2,000 focal mechanisms for each target event based on bootstrap resampling of the amplitude ratio

240 data. The difference between the focal mechanisms and the best solution was measured
241 using the 3-D rotation angle (Kagan, 1991). We discarded the results if the 95%
242 confidence interval was greater than 30°.

243 The analyzed frequency range must be smaller than the source corner frequencies
244 of both the target and reference events. We first used a frequency range of 0.8–2.0 Hz
245 to estimate the moment tensors for M_{JMA} 2–4 events. We used the F-net moment tensor
246 catalog (Kubo et al., 2002) to select the reference events. We adopted 217 events with
247 $3.5 < M_w < 4.0$ and values of variance reduction greater than 70% (Figs. 3a and d). Using
248 these events as references at the relocated locations, we obtained moment tensor
249 solutions for 7,952 M_{JMA} 2–4 events, including 6,683 events with an M_w of 3 or less
250 (Figs. 3b and e).

251 Next, to derive the moment tensors for smaller events, we used $M_w < 3$ events, for
252 which the moment tensors were estimated (Fig. 3b) as reference events. Only events
253 with a 95% confidence range smaller than 25° are adopted as reference events. We
254 selected a frequency band of 2–5 Hz, which provided sufficient S/N for events in this
255 magnitude range. As a result, we newly derived moment tensors for 23,811 events with
256 a 95% confidence range of less than 30° (Figs. 4c and f). Of these, 2,340 events have an
257 M_w of 1.7 or less, which are used in the following analysis.

258 Figures 3(b) and (c) show the spatial distribution of the moment tensors in the
259 first and second processes, respectively. The results show that most events in this
260 region have normal fault-type focal mechanisms, which is consistent with the typical
261 fault type in this region (Fig. 1a; Kato et al., 2011; Yoshida et al., 2015).

262

263

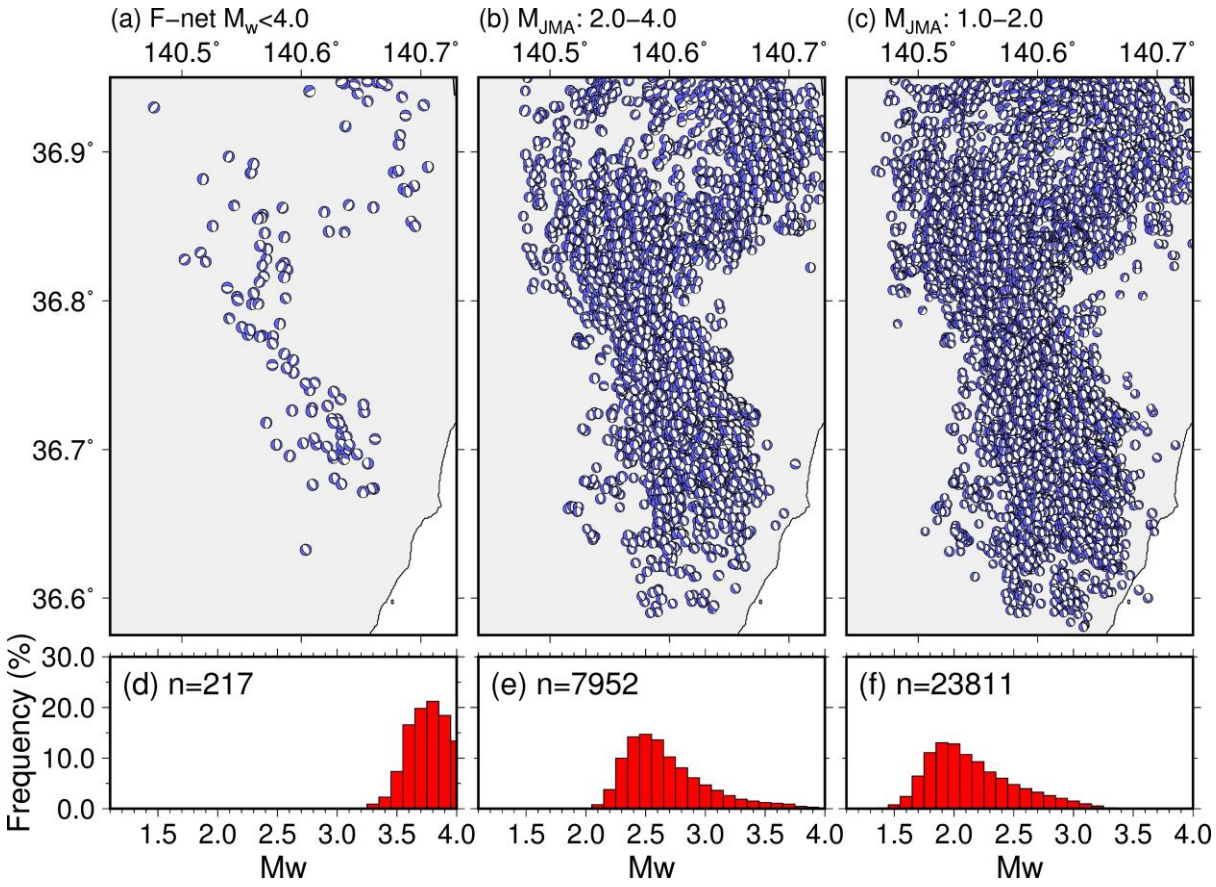

Figure 3. Moment tensor solutions. (a): reference events with 3.5 < M_w < 4.0 and variance reduction greater than 70% from the F-net catalog (n=217). Locations of the F-net focal mechanism are shifted in the relocation results. (b): Events with M_{JMA} 2.0–4.0 whose moment tensors were determined by the first processing (n=7,952). (c): Events with M_{JMA} 1.0–2.0 whose moment tensors were determined by the second processing (n=23,811). (d), (e), and (f): histograms of M_w for the datasets in (a), (b), (c), respectively.

3. Comparison between observed and synthetic waveforms

3.1. Computation of synthetic waveforms

We estimated the Q-structure by comparing the observed waveforms obtained at the downhole sensor of the N.JUOH station with those of its synthetic counterparts. We must assume a tentative Q-structure to compute the synthetic Green's functions. We use Brocher's (2008) empirical relationship to assume the Q-value, following previous studies (e.g., Yamaya et al., 2022). Density was determined from the P-wave velocity

(Ludwig et al., 1970) as follows:

$$\rho(\mathrm{g/cm^3}) = 1.6612\mathrm{Vp} - 0.4721\mathrm{Vp}^2 + 0.0671\mathrm{Vp}^3 - 0.0043\mathrm{Vp}^4 + 0.000106\mathrm{Vp}^5 \quad . \tag{2}$$

The Q_p (Q of the P-wave) and Q_s (Q of the S-wave) were determined from the S-wave velocity as follows:

$$Q_s = -16 + 104.13\mathrm{V_s} - 25.225\mathrm{V_s^2} + 8.2184\mathrm{V_s^3} \tag{3}$$

$$Q_s = 13 \text{ for } \mathrm{V_s} < 0.3\,\mathrm{km/s} \tag{4}$$

$$Q_p = 2Q_s \quad . \tag{5}$$

The depth profiles of the density, Q_p, and Q_s are shown in Fig. 2(c) and (d).

We computed Green's functions using the code of Zhu and Rivera (2002) based on the wavenumber integration method. We chose a frequency range of 5–20 Hz. We only use events with $M_\mathrm{w} \leq 1.7$ and set the source duration for the synthetic waveform calculation to 0.01 s (triangle), which is short enough for the analysis bandwidth. Note that the actual source durations of these events are diverse, but the low-pass filter removed that information. We use the moment tensor solutions obtained in Section 2. However, synthetic waveforms sometimes do not explain the polarities of the observed waveforms well because of errors in the moment tensors. We modified the focal mechanisms slightly to better explain the observed three-component waveforms at the N.JUOH station. In particular, we conducted a grid search for the double-couple moment tensor (Fig. S2), within 35 °of the 3-D rotation angle (Kagan, 1991) of the previous solution. A low frequency of 1.2–3.0 Hz is used to avoid the attenuation effects. We removed results with poor agreement between the synthetic and observed waveforms (variance reduction < 50%), leaving 1,006 events (Fig. S3). M_w was, on average, 0.4 larger than M_JMA for these events (Fig. S4). The tendency of M_w to be larger than the M_JMA for small (M_w < 3) events has been reported in previous studies in this region (Uchide & Imanishi, 2016) and other regions of Japan (Edwards and Rietbrock, 2009; Yoshida et al., 2017) as well.

Figure 4 shows the synthetic waveforms (displacements; f < 25 Hz), the patterns of which agree well with the observed waveforms. We computed the cross-correlation coefficient between each pair of observed and synthetic waveforms for the 2–10 Hz frequency interval. The median values for the vertical, radial, and transverse

components were 0.75, 0.73, and 0.75, respectively (Fig. S5). In the observed transverse component waveforms, direct waves were sometimes followed by large-amplitude waves that were not observed in the synthetic waveforms, which may have been affected by unmodeled factors. Hereafter, we refer to the vertical component.

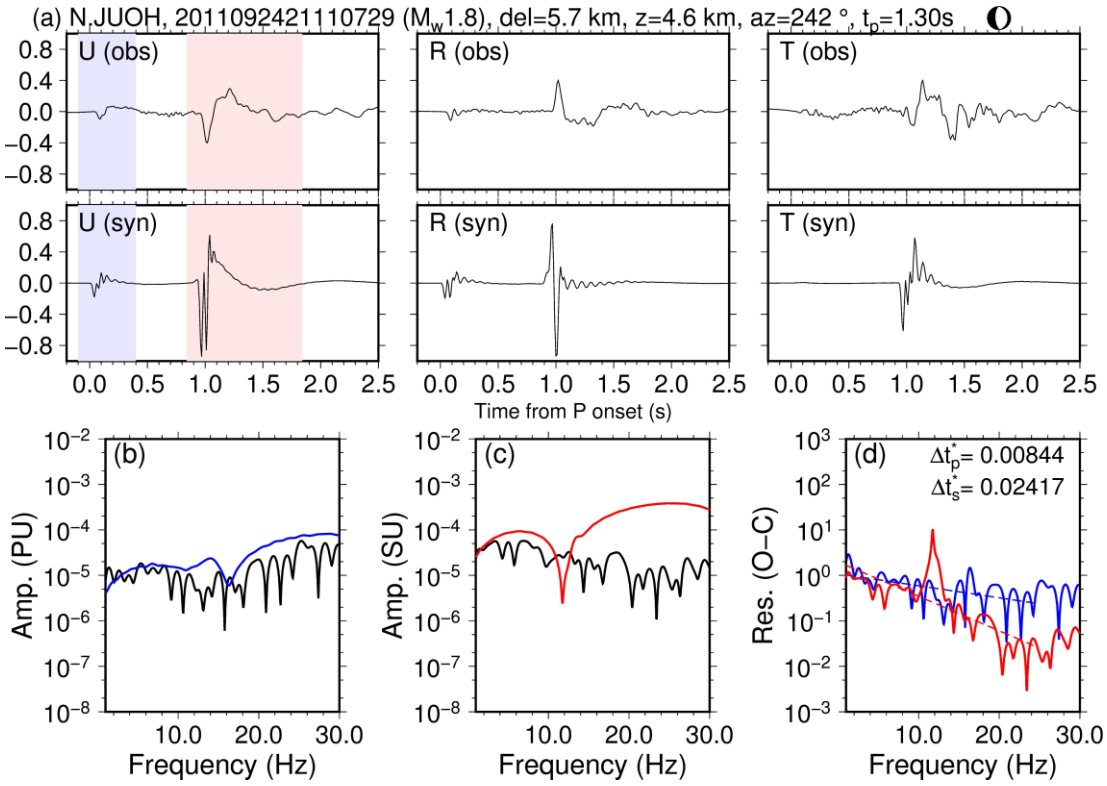

Figure 4. Comparison of observed and synthetic waveforms (displacement waveform). (a) Observed (above) and synthetic waveform (below) for vertical (left), radial (center), and transverse (right) components. (b), and (c): comparison of observed and synthetic spectra for the vertical components of P- and S-waves, respectively. (d) Residuals between observed and synthetic spectra. The blue curve shows the P-wave, and the red curve shows the S-wave. The dashed lines represent the fitted lines.

The Q-model assumed above is based on an empirical relationship with seismic wave velocities. The Q-model was refined based on the spectral discrepancies. We cut the P- and S-wave windows from the observed and synthetic waveforms. Their spectra were computed using the FFT algorithm, as shown in Figs 4(b) and (c). The P-wave

window is cut from 0.1 s before the arrival to 0.5 s after, and the S-wave window is cut from 0.1 s before the arrival to 1.0 s after. We computed the logarithmic residuals of the observed spectra $O_i(f)$ and synthetic spectra $S_i(f)$ of the i-th event as follows:

$$\ln R_i(f) = \ln O_i(f) - \ln S_i(f). \quad (6)$$

Figure 4(d) shows an example. We used the residual spectrum $R_i(f)$ to refine our 1-D Q-model. If the assumed Q-model is appropriate, $\ln R_i(f)$ should be close to 0; however, if the assumed Q-model is inappropriate, $\ln R_i(f)$ can differ substantially from 0.

3.2. Frequency dependence of residual spectra

We aim to estimate $\Delta(Q^{-1}(z)) = Q_{\mathrm{mod}}^{-1}(z) - Q_{\mathrm{org}}^{-1}(z)$, the difference between the assumed Q^{-1}-model ($Q_{\mathrm{org}}^{-1}(z)$) and the optimal one ($Q_{\mathrm{mod}}^{-1}(z)$), where z is depth. First, we examined the frequency-dependent trend of $R_i(f)$. If $\Delta(Q^{-1}(z))$ does not depend on frequency and depth, $\ln R_{\mathrm{i}}(f)$ changes with f in proportion to $-\pi\Delta(Q^{-1})t_0 f$ (Eq. 1), where t_0 is travel time. We measure the slope, a, of $\ln R_{\mathrm{i}}(f)$ in the range of 2–20 Hz (Fig. 4d), and obtain $\Delta t^* = -a/\pi$, which represents $\Delta(Q^{-1})t_0$, for each event. Figures 5(a) and (c) show the histograms of Δt^* for the P-wave (Δt_p^*) and S-wave (Δt_s^*). Δt_s^* is positive in almost all cases (99%), with a median value of 0.0123. The median 95% confidence range of Δt_s^* estimated by bootstrapping is 0.0118 to 0.0127. The significantly positive value suggests that the actual attenuation is stronger at higher frequencies than predicted by the model (i.e., $\Delta(Q^{-1})$ is positive). In the case of P-waves, the median of Δt_p^* is approximately 0.0023, with the median 95% confidence interval ranging from 0.0117 to 0.0127. There are many events with negative Δt_p^* (33%). Still, in both P- and S-waves, Δt^* tends to increase as the horizontal distance increases (Figs. 5b and d).

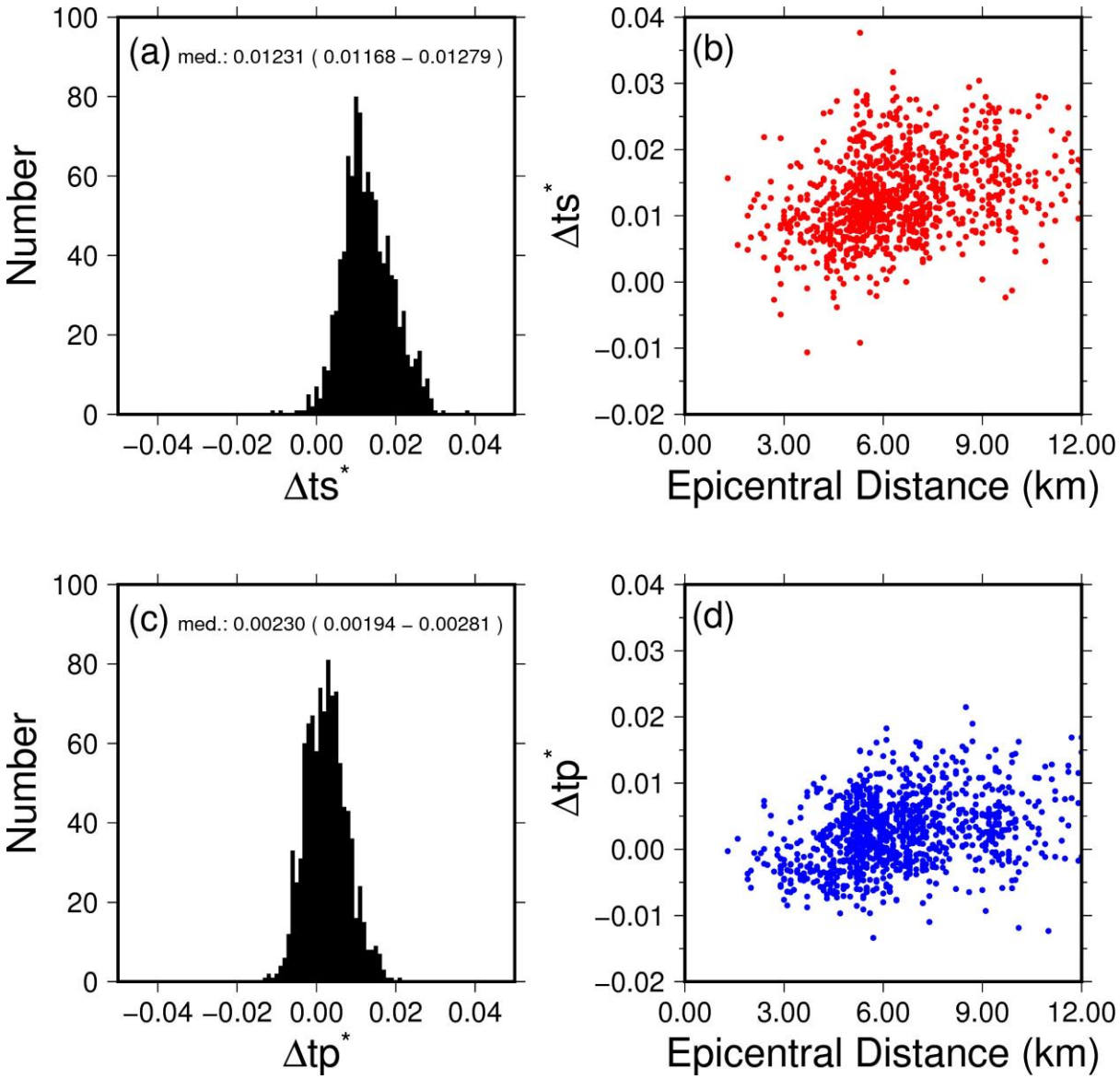

Figure 5. Characteristics of Δt^*. (a) and (b): Δt_s^* and Δt_p^*, respectively. (c) and (d): Δt_s^* and Δt_p^*, respectively, versus epicentral distance.

We computed that $\Delta q^{-1} = \Delta t^*/t_0$. Δq^{-1} coincides with $\Delta(Q^{-1})$ when $\Delta(Q^{-1})$ is constant in frequency and has no spatial variation. Figures 6(a) and (c) show the histograms of $\Delta q^{-1} =$ for P-wave (Δq_p^{-1}) and S-wave (Δq_s^{-1}). The median value of Δq_s^{-1} is approximately 0.0039 and shows no clear horizontal distance dependence (Fig. 6b). This suggests that the horizontal distance dependence observed in Δt_s^* is essentially explained by the increasing total attenuation due to increasing propagation distance. If we use $Q_{\mathrm{org}} = 350$ for the depth-average initial Q_{org}^{-1}-value (Fig. 3c), we obtain

$Q_s = 1/(Q_{org\_s}^{-1} + \Delta q_s^{-1}) = 148$. For the P-wave, Δq_p^{-1} was distributed around 0 (Fig. 6c), but the median value is positive (0.0013). If we use $Q_{org} = 700$ for the depth-average initial Q_{org}-value (Fig. 3c), we obtain $Q_p = 1/(Q_{org\_p}^{-1} + \Delta q_p^{-1}) = 366$.

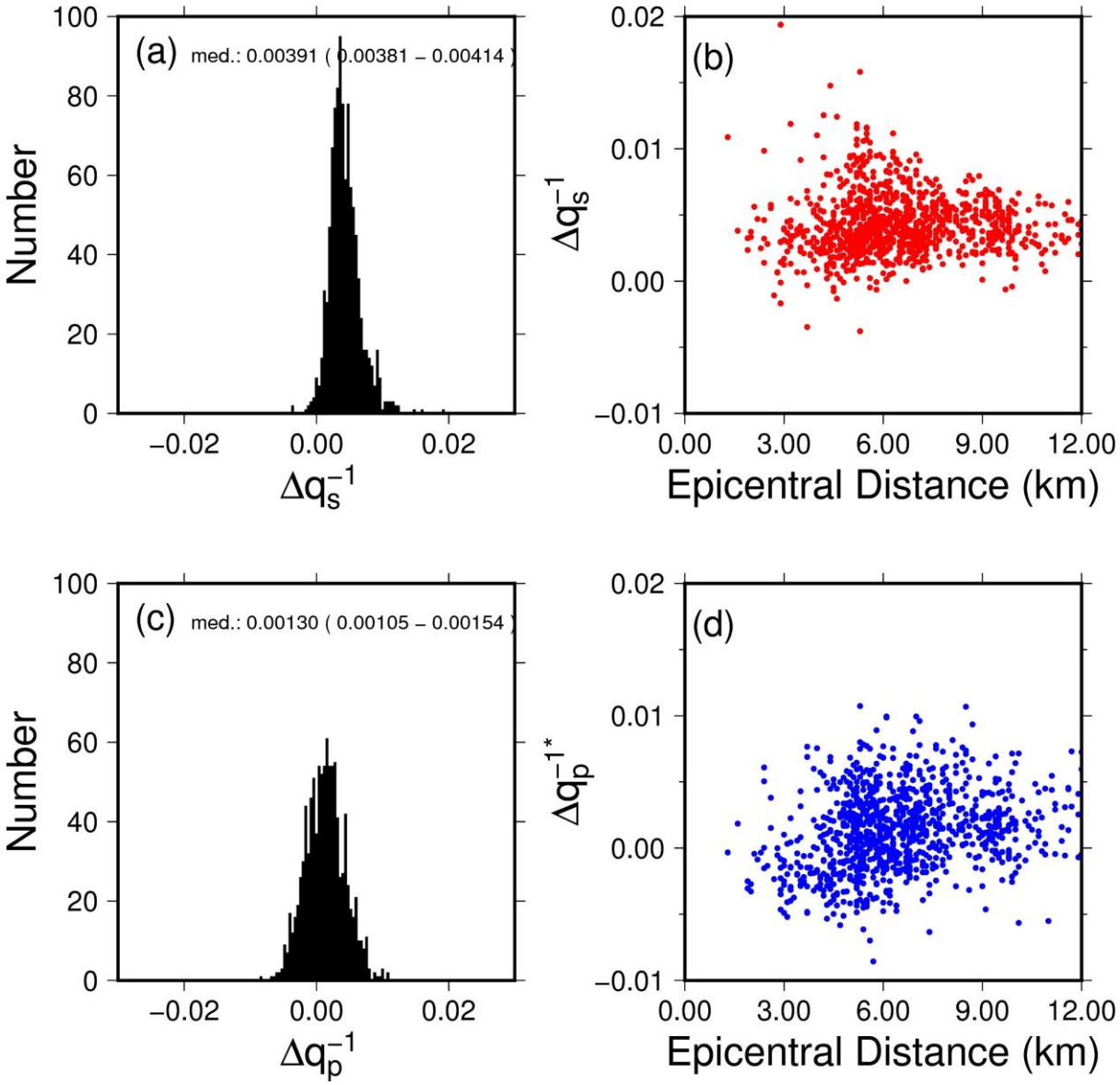

Figure 6. Characteristics of Δq^{-1}. (a) and (c): Histograms of Δq^{-1} of S- and P-waves, respectively. (b) and (d): Δq^{-1} versus lateral distance for the S- and P-waves, respectively.

4. Estimation of Q-structure and radiated energies of small events

4.1. Refinement of the Q-model

In the previous section, we made a rough estimate of the Q-value, assuming that the $\Delta(Q^{-1})$ is constant along the path and independent of frequency. We here eliminate the above assumptions and estimate depth-dependent $\Delta(Q^{-1}(f))$ and Q-value. We divided the frequency range into five bands: (1) 5–8, (2) 8–11, (3) 11–14, (4) 14–17, and (5) 17–20 Hz. To avoid the influence of subtle errors in the focal mechanisms on the spectral amplitudes, we multiplied the amplitudes of the synthetic spectra by a constant, such that the mean amplitudes of the synthetic and observed spectra matched at low frequencies (1.5–3 Hz). We compute the mean value of $\ln R_i(f)$ in the k-th frequency band for each event r_{ik}.

Figures 7(a), (c), (e), (g), (i), (k), (m), (p), (q), and (s) compare the r_{ik} of the 1,006 events with epicentral distances for the P- and S-waves. The red line represents the average value of r_{ik} of different events. r_{ik} is scattered but tends to significantly decrease with increasing distance at high (> 14 Hz) frequencies, especially for the S-wave. At f > 14 Hz (Figs. 7a and e), r_{ik} is as small as -2 for the S-wave, even at short distances. The same tendency is observed for the P-wave, although not as pronounced as that for the S-wave. These trends suggest that the observed spectra $O_i(f)$ are subject to stronger attenuation than the modeled spectra $S_i(f)$.

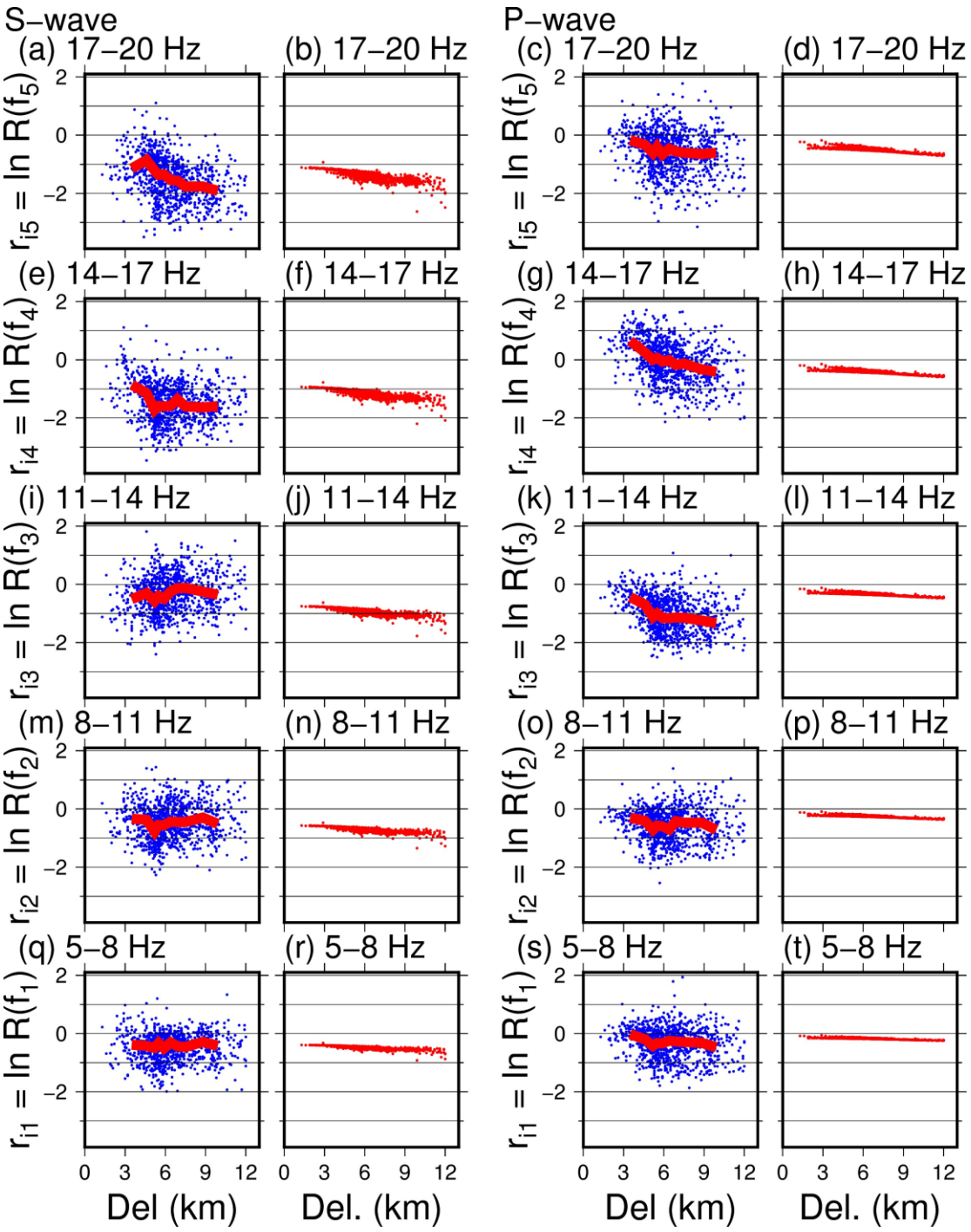

Figure 7. Relationship of the spectral residuals $\ln R_i(f)$ with the epicentral distance. (a), (c), (e), (g), (i), (k), (m), (o), (q), and (s) show the observed $\ln R_i(f)$ for different frequency windows and wave types. The red line represents the average value. (b), (d), (f), (h), (j), (l), (n), (p), (r), and (t) show the relationship between the residuals and the distance expected for the estimated Q-structure shown in Fig. 8.

If the $M_w \leq 1.7$ events used included those with corner frequencies smaller than the respective frequency bands, $\ln R_i(f)$ should be smaller than 0 for them due to the source finiteness effects. However, the high-frequency residuals are larger not only in some of those outliers but, on average, than would be inferred from the ω^2-model. Moreover, the distance attenuation observed in our results cannot be explained by the source finiteness of small events, which indicates that the obtained residual trends are due to the attenuation effects during wave propagation.

We modify the Q-value of each layer for each frequency band such that the synthetic spectral amplitudes agreed better with their observed counterparts. We refer to the original Q-value at the j-th layer as $Q_{\mathrm{org\_j}}^{-1}(f)$ and the modified Q-structure as $Q_{\mathrm{mod\_j}}^{-1}(f)$, and attempt to estimate $\Delta(Q_{\mathrm{j}}^{-1}(f)) = Q_{\mathrm{mod\_j}}^{-1}(f) - Q_{\mathrm{org\_j}}^{-1}(f)$. Using the time Δt_{ij} required for the direct wave of the i-th event to pass through the j-th layer, r_{ik} can be related to $\Delta(Q_{\mathrm{j}}^{-1}(f))$ as follows:

$$r_{\mathrm{ik}} = -\pi f \sum_{\mathrm{j}=1}^{\mathrm{n_{lay}}} \Delta(Q_{\mathrm{j}}^{-1}(f_{\mathrm{k}}))\Delta t_{\mathrm{ij}}, \quad (6)$$

where f_{k} is the mean frequency of the kth frequency band, and $\mathrm{n_{lay}} = 16$ is the number of layers. Using equations from multiple events (number: $\mathrm{n_{eve}} = 1006$), we write this equation system in vector form for each frequency band (i.e., k fixed) as follows:

$$\boldsymbol{r}_{\mathrm{k}} = -\pi f T \boldsymbol{m}_{\mathrm{k}}, \quad (7)$$

where $\boldsymbol{r}_{\mathrm{k}}$ is a vector of $\mathrm{n_{eve}}$-raw, containing r_{ik} $(\mathrm{i} = 1, \cdots, n_{\mathrm{eve}})$, $\boldsymbol{m}_{\mathrm{k}}$ is a vector of $\mathrm{n_{lay}}$-raw containing $\Delta Q_{\mathrm{j}}^{-1}(f_{\mathrm{k}})$ $(\mathrm{j} = 1, \cdots, n_{\mathrm{lay}})$, and $T = (\Delta t_{\mathrm{ij}})$. We calculate Δt_{ij} based on the hypocenters and velocity structure shown in Fig. 3(b). $\boldsymbol{m}_{\mathrm{k}}$ was solved using the damped least-squares method, with the damping parameter determined by the tradeoff curve with the residuals. Through trial and error, we found that an adjustment of the Q-values in the four shallow (z < 4.2 km) layers was almost sufficient to explain our data. Therefore, to avoid instability, we increased the damping factor of the deeper layers by a factor of five over that of the shallower layers and focused on the changes in the shallow layers.

Figure 8 shows the obtained 1-D Q-model ($Q_{\mathrm{mod_j}}^{-1}(f_{\mathrm{k}})$) for 17–20 Hz ($k = 5$) for the P- and S-waves. The mean values of Q_s and Q_p at depths < 4 km were approximately 55 and 105, respectively ($Q_{\mathrm{p}}/Q_{\mathrm{s}} = 1.9$), which were much smaller than the original

values at depths shallower than 4 km ($Q_s = 350,\ Q_p = 700$). The modification of the Q-model reduces the RMS residual from 1.65 to 0.68 for the S-wave and 0.88 to 0.70 for the P-wave. In the second layer, at a depth of 10–110 m, the obtained Q-value was high ($Q_s = 250,\ Q_p = 509$), but the time elapsed through this layer was so short that it had little effect on the spectral amplitudes. This high value is apparent because of the damping to the initial value. Therefore, we changed the Q_s- and Q_p-values for the second layer to the same values as those for the 0–10 m depth ($Q_s = 34,\ Q_p = 69$). These changes in residuals were less than 0.01%, and the residuals were rather reduced.

Figures 7(b), (d), (f), (h), (j), (l), (n), (p), (r), and (t) show the distance dependence of the calculated r_{ik} when the actual Q-structures are as shown in Fig. 8 (17–20 Hz). The refined Q-model reproduces the decreasing trend with observed distance well due to this low Q-value. The result that the actual Q-value is much smaller than the assumed initial model is consistent with the results based on the frequency-dependent amplitude decay in Subsection 3.2. However, the specific Q-values obtained here are lower than the estimates in Subsection 3.2 from the frequency-dependent amplitude decay ($Q_{\mathrm{s}} = 148, Q_{\mathrm{p}} = 366$) at shallow depths. The results obtained in this study, which do not pre-suppose a specific frequency dependence of Q, are deemed more reasonable than those assuming a constant Q-value in both frequency and space.

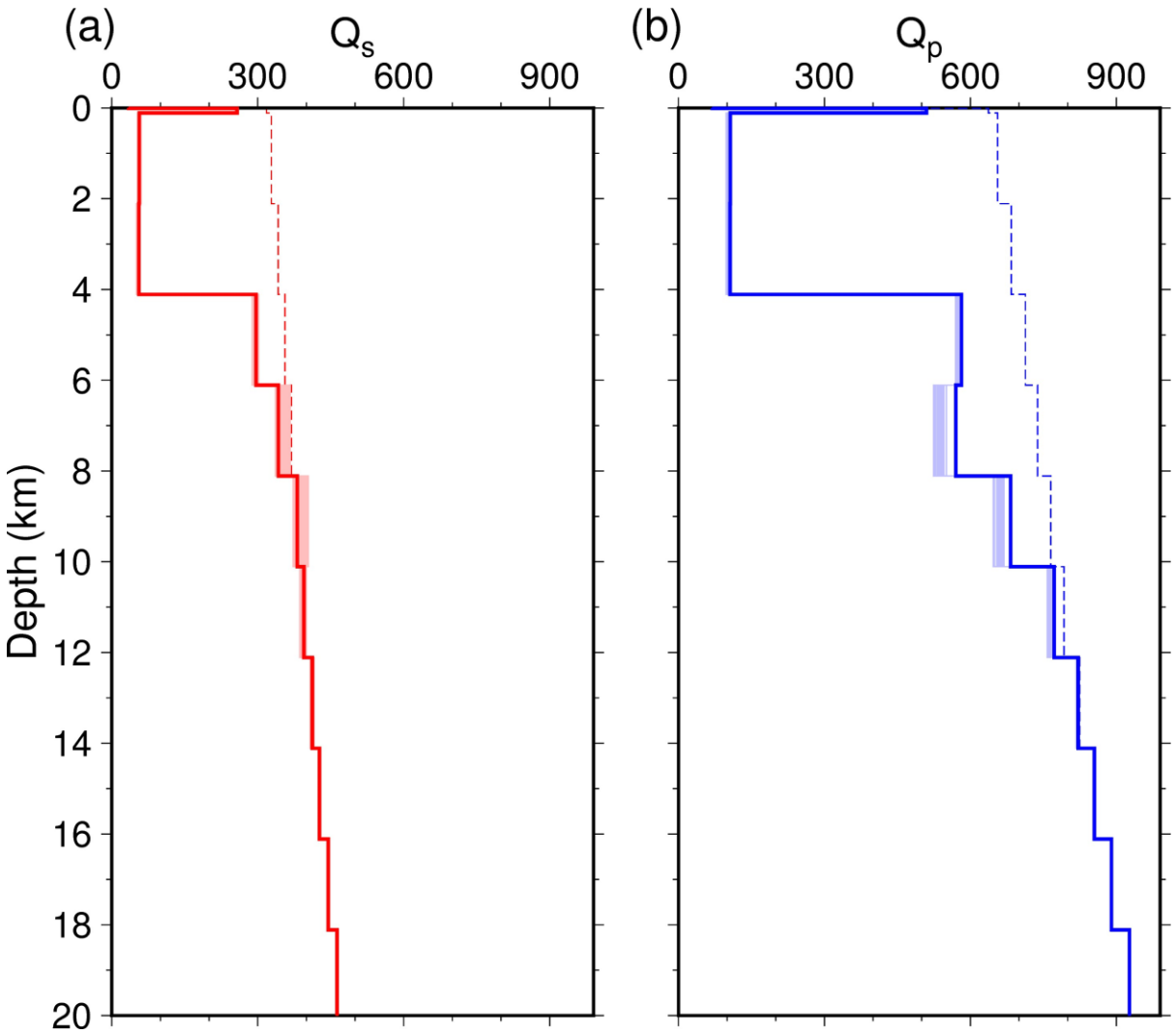

Figure 8. Estimated Q-structure (17–20 Hz). (a) Q_p and (b) Q_s. The solid and dashed lines represent the derived and initial models, respectively. The light-colored lines indicate the 1,000 results based on bootstrap resampling.

We performed 1,000 bootstrap samplings of the events to estimate the uncertainty in the Q-values and obtained 1,000 results (Fig. 8). Uncertainties in the Q-values were small at depths shallower than 4 km. Most waves pass through a layer shallower than 10 km (Fig. S6), and the results for the deeper layers were not reliable. The Q-values estimated at different frequencies and predicted residuals are shown in Figs. S7 and S8. The Q-values varied with the frequency band. However, in the lower-frequency bands, the influence of the assumed Q-structure is small, owing to the short distances. Note that even at a constant Q-value, the attenuation is stronger at higher frequencies (Eq.

1). Even when using the Q-values obtained for the 17–20 Hz range, the features on the lower-frequency side appear to be roughly explained (Fig. 7). The mean RMS residuals increase only from 0.62 to 0.71 for the S-wave (1.08 for the initial model) and from 0.61 to 0.73 for the P-wave (0.83 for the initial model) even if we use the Q-values obtained for the 17–20 Hz range in the entire frequency band.

4.2. Radiated energy of small events

Based on the refined Q-model, we estimated the radiated energies of the M_w 2.0–4.5 events for which we obtained moment tensor solutions (Figs. 3a and b). We used the Q-model obtained at 17–20 Hz for the entire frequency band because this model generally explains the trend for all frequencies (Fig. 8). We only included events within an epicentral distance of 12 km and used waveforms obtained at a single near-source station (N.JUOH). Although the radiation patterns of earthquakes become obscure with increasing frequency and distance (Takemura et al., 2009), at near-source distances, the radiation patterns are preserved even at high frequencies (Trugman et al., 2021). The data are the vertical components of the S-wave at the N.JUOH station because of the synthetic fitness (see Fig. 4). We remove the instrumental response and use the frequency range of $f < f_h$=25 Hz.

To account for the wave propagation effects, we used synthetic waveforms. We recomputed the synthetic waveform based on the refined Q-model for each target event with a source duration of 0.01 s, unit seismic moment, and the same focal mechanism as the target event. The duration is sufficiently short from the upper limit of the analyzed frequency band, in which the synthetic waveforms have only information on wave propagations and focal mechanisms.

We estimated the moment rate spectrum $\dot{M}(f)$, by dividing the spectral amplitudes of each observed waveform by those of the synthetic waveform. We estimated the radiated energy from $\dot{M}(f)$ based on Vassiliou and Kanamori (1982):

$$E_R = 8\pi \left(\frac{1}{15\rho\alpha^5} + \frac{1}{10\rho\beta^5}\right) \int f^2 \dot{M}^2(f) df \quad (3),$$

where ρ is the density, α is the P-wave velocity, and β is the S-wave velocity at the

source. High-frequency amplitudes above high-cut frequency f_h=25 Hz are corrected based on the method of Snoke (1987). This method assumes that the amplitude decreases in proportion to f^{-2} at higher frequencies than f_h.

We obtained E_R for 3,884 events with M_w 2.0–4.5. As the estimates are based on a single station, individual estimates are strongly affected by rupture directivity (Venkataraman & Kanamori, 2006; Yoshida, 2019). Therefore, we focused on the statistical characteristics. Figure 9(a) shows the $e_R = E_R/M_0$ for the 3,884 events. The median e_R for the events is 3.6×10^{-5}, which is similar to the median values (3×10^{-5}) obtained in the crust of Japan by Kanamori et al. (2020) and Yoshida and Kanamori (2023) for larger events (M_w > 5.6 and M_w > 3.0, respectively). This value is similar to those estimated for earthquakes worldwide (e.g., Ide & Beroza, 2001).

Figure 9(b) shows the relationship between e_R and M_w. We divided the dataset into 20 bins according to M_w and computed the median values for each bin with the same number of e_R data and the 95% significance intervals using 1,000 bootstrap resamplings. The results do not show a clear scale-dependent trend in the M_w 2.0–4.5 range. Upon closer inspection, it appears that the e_R increases slightly with M_w between the M_w 2.5–3.5 events. However, the frequency range we were able to use is up to f_h=25 Hz, beyond which we extrapolated the source spectra using the ω^2-model (Snoke, 1987). The effect of correction is greater for smaller events as they have higher dominant frequencies, making it difficult to discuss this slight difference (< 30 %). The depth dependence of the source parameters is controversial (Abercrombie et al., 2021), but our estimated e_R is almost depth-independent at depths from 3 to 10 km (Fig. 9c).

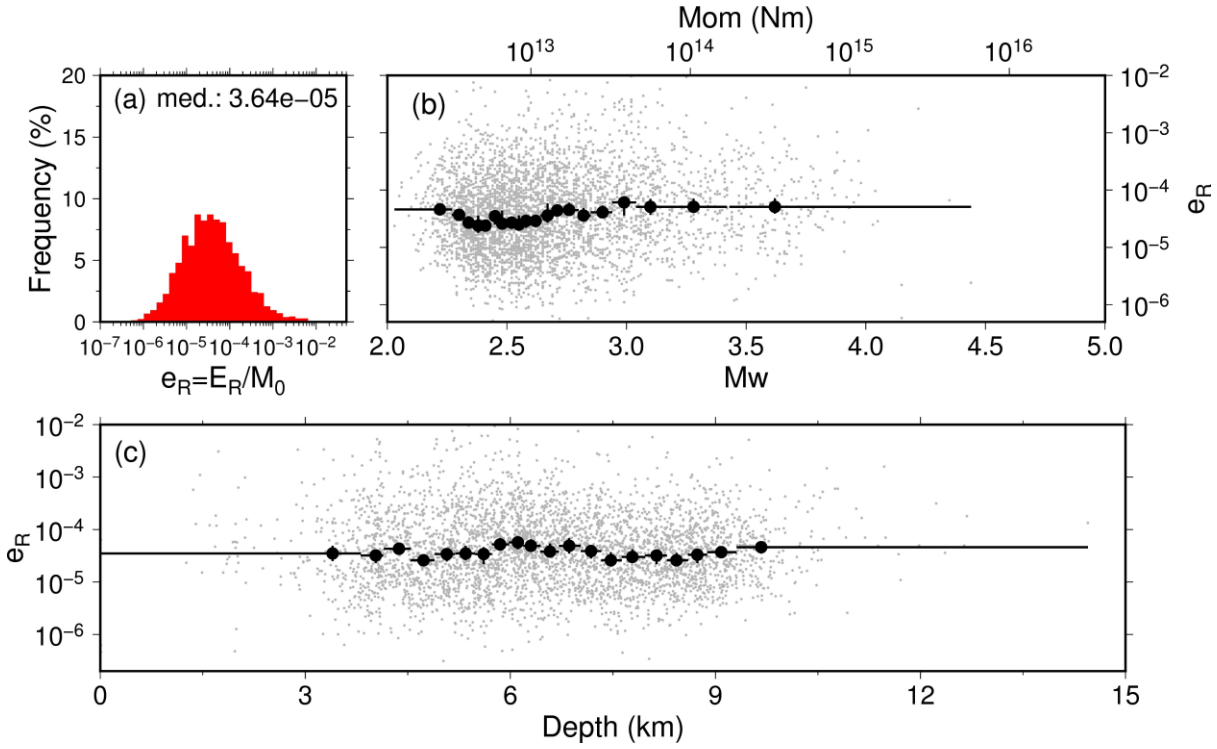

527
528

529 **Figure 9.** Results of scaled energy e_R. (a): Histograms of e_R. (b) and (c): e_R compared
530 with moment magnitude M_w, and depth, respectively. Small gray circles represent
531 individual results; large circles represent the median of each M_w range. The vertical
532 line represents the 95% confidence range of the median value. The horizontal line
533 represents the M_w range.

534

535 **5. Discussion**

536 We obtained small Q_s-values for the shallow (< 4 km) crust, averaging ~55,
537 based on a comparison of observed and synthetic seismic waveforms of events with M_w
538 < 1.7. The use of near-source waveforms at a hard rock site allowed us to confirm that
539 the shapes of the observed and synthetic waveforms were similar and did not include
540 distinct reflected or converted waves, which were not considered in the model. In
541 estimating the Q-value, many previous studies used various assumptions about the
542 source spectra, such as the ω^2-model and negligible effects of rupture directivity, and
543 Q-condition, such as spatially uniform and/or constant regardless of frequency.
544 However, we did not make these assumptions. Our only assumption is that at f < 20Hz,
545 the duration of the moment rate function for M_w < 1.7 events is small enough to be

546 considered a delta function (i.e., flat spectral amplitude). Using the obtained Q_s-model,
547 we estimated the moment-scaled seismic radiated energy, $e_R = E_R/M_0$, for more than
548 3,884 events with M_w 2.0–4.5 and obtained a median value of 3.6×10^{-5}, similar to that
549 estimated for M_w > 6 earthquakes in Japan (Kanamori et al., 2020), without obvious
550 scale dependence.

551 Previous studies examined the frequency dependence of the Q_s-value by
552 assuming a spatially uniform Q_s condition. It has been suggested that the Q_s-value
553 increases proportionally with frequency ($Q \propto f^n$, $n = 1$) in the upper lithosphere (e.g.,
554 Sato et al., 2012). In such situations, the spectral amplitudes of the high- and
555 low-frequency components decrease by the same amount during wave propagation (Eq.
556 1). Therefore, the high-frequency amplitude did not decay faster than the
557 low-frequency amplitude. However, our results show stronger attenuation at higher
558 frequencies. Some studies obtained smaller values of $n = 0.6 - 0.9$ (Aki, 1980;
559 Kinoshita, 1994; Moya & Irikura, 2003; Oth et al., 2010), in which case the attenuation
560 effect becomes slightly stronger at higher frequencies. However, our observations are
561 essentially explained even when a constant Q_s-value of ~55 is assumed at 1–20 Hz (Fig.
562 7). If Q_s-values in the study region significantly increase with frequency, the Q_s-value
563 at low frequencies needs to be unrealistically small (~12 at 1 Hz for $n = 0.6$ and ~4 for
564 $n = 1$). This suggests that, in the shallow crust of this region, Q_s increases much more
565 slowly than f.

566 Owing to the various assumptions in estimating Q-value in different studies, it is
567 not straightforward to directly compare the results. In several regions of the upper
568 lithosphere of Japan, Q_s-values have been estimated using different methods and
569 assumptions; Yoshimoto et al. (1993), Takahashi et al. (2005), and Yoshida et al.
570 (2017) used the coda normalization method of Aki (1980) and obtained Q_s-values of >
571 300 at 20 Hz. These studies essentially assumed spatially uniform Q_s-values and
572 examined the distance decay of seismic wave amplitudes at relatively long distances (>
573 20 km) outside particular source regions. Their Q_s-estimates were much larger than
574 those of the shallow crust in this study ($Q_s = 55$), possibly because of the different
575 depth sensitivities between their analysis and ours. The seismic waves used in their

analyses mainly propagated at depths > 10 km because of large epicentral distances, and the distance decays were more strongly affected by attenuation at deep levels. In contrast, the present study only used records with epicentral distances less than 12 km from shallow (<10 km) events, and the results essentially represented shallow structures. The difference in these estimates may indicate that the shallow Q_S-value is much smaller than the deep Q_S-value. Yoshida et al. (2017) reported that their Q_S^{-1}-model based on the distance decay of waveform amplitudes, was insufficient to explain the observed high-frequency energy loss of earthquake spectra event at a hard-rock site. They suggested that stronger attenuation exists in the shallow crust.

To observe the effect of strong depth variations in Q-values on the distance decay of seismic wave amplitudes, we examined synthetic waveforms based on our refined model. We assume a normal-fault event (strike of 90°, dip of 45°, and rake of -90°) with M_w of 4 and source duration of 0.01 s (triangle) as the source. Synthetic waveforms were computed at epicentral distances ranging from 2 km to 100 km, with station azimuths of 15°, 30°, and 45°, given the symmetry of the radiation pattern. We calculated the S-wave spectra 0.3 s before the arrival to 4.0 s after and obtained the median amplitude, A, in the 17–20 Hz band, and multiplied them by the propagation distances, r, to remove the effects of geometrical spreading by assuming $\gamma = 1$ in Eq. (1). Figure 10(a) compares travel time t with Ar for the vertical component, showing a weak decreasing trend owing to Q. For comparison, we also calculated the amplitude attenuation for two uniform Q-values (Q_S=400 and Q_S=55) based on Eq. (1). The overall distance decay pattern of the synthetic waveform amplitudes appeared to follow the prediction from a uniform value of Q_S=400, corresponding to the average value on the deeper side (> 8 km). If we fit Eq. (1) to the synthetic amplitudes by assuming a uniform Q_S-value, we obtain Q_S=443, although Q_S is approximately 55 on the shallow (< 4 km) side of the model used. Figure 10(b) shows the S-wave amplitudes based on the reference model (Q_S-value of approximately 350 for depths < 4 km), whose decay pattern is similar to that of the revised model (Fig. 10a). If we fit Eq. (1), we obtained Q_S=516. The results for the radial and transverse components show a similar trend (Fig. S9). These results indicate that the distance decay of the seismic amplitude at far

distances (> 30 km) is greatly affected by the deep Q-value and does not provide much information on the shallow Q-value. However, such a small Q-value at a shallow level strongly affects the estimation of the source parameters for small events.

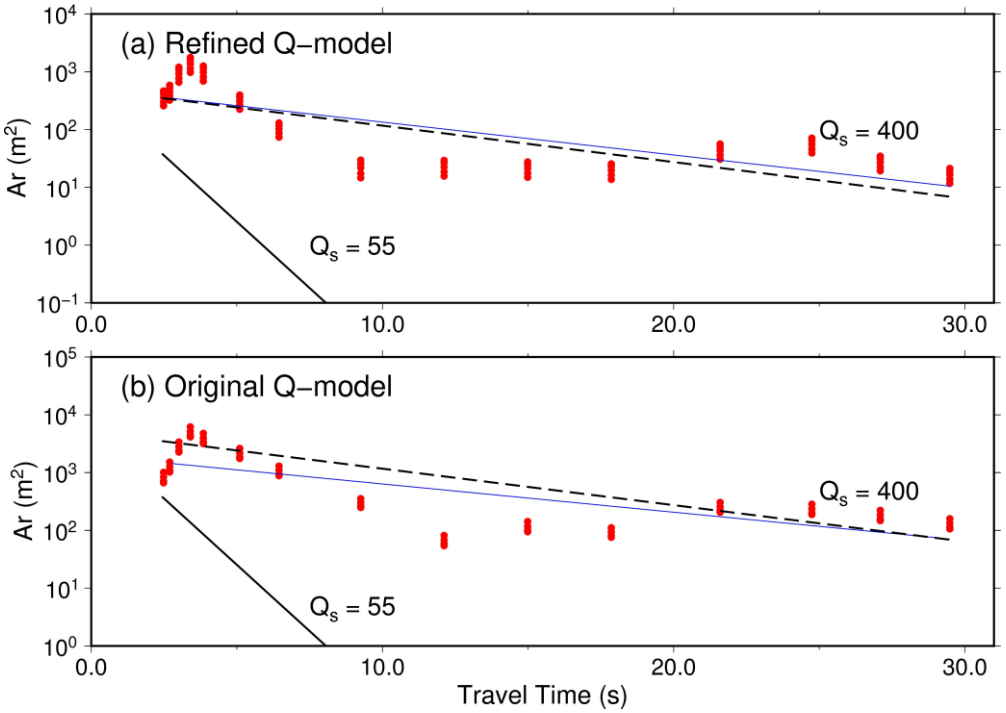

Figure 10. Amplitude decay of the synthetic waveforms against travel time. (a) Results based on the refined model (Fig. 8a), and (b) results based on the original model (Fig. 2c) for three different station azimuths. Circles show the median spectral amplitudes of the synthetic waveforms in the 17–20 Hz band. Black solid and broken lines show the distance decay pattern predicted from models with $Q_s = 400$ and $Q_s = 55$, respectively, independent of depth. The blue line shows the result obtained by fitting Eq. (1) to the observed data.

A possible reason for the low Q_s-value in the shallow crust of the study region is that it is seismically active. Faults and fracture zones exist (Kato et al., 2013; Yoshida et al., 2015), and seismic waves may attenuate as they pass through them. Abercrombie (2000) showed that Q-varies greatly with rock type and that the Q-value in fault zones may be small (Q_p=50, Q_s=80). Estimations using trapped waves in the fault zone also

indicated that the Q-value in the fault zone can be very small (Qiu et al., 2017). Additionally, previous studies have suggested that fluids exist in fault zones in this region and affect the intense seismicity (Kato et al., 2013; Umeda et al., 2015; Yoshida et al., 2015; Zhao et al., 2015; Usuda et al., 2021). Yoshida (2021) examined the seismic waves in a fluid-driven earthquake swarm in Japan and suggested that the near-source (< a few kilometers) Q_s-value was very small (< 50) during intense fluid migration. The presence of fluid may have resulted in small Q_s-values in this region.

Alternatively, such a low Q-value may not be uncommon in shallow crust. Hauksson et al. (1987), using deep borehole records, derived a similar value of $Q_s = 30$ at a depth of 0.4–1.5 km in the Newport-Inglewood fault zone, Los Angeles basin. Similarly, many previous studies have shown that Q-value is very small at shallow depths (Anderson, 1986; Frankel, 1992; Kinoshita & Ohike, 2002; Fukushima et al., 2016). Many of the aforementioned studies assumed that Q-value is constant in frequency, with a small value indicating that the observed amplitudes are strongly attenuated at higher frequencies. Such strong shallow attenuation is sometimes treated separately from the average Q, and referred to as κ (Anderson & Hough, 1984; Edwards et al., 2015; Hassani & Atkinson, 2018). Although such reports are often made for sedimentary layers, Abercrombie (1995) obtained a small value (~20) at a depth of < 3 km from the Cajon Pass borehole stations in southern California. Hauksson and Shearer (2006) obtained Q_{p}- and Q_{s}-values of approximately 100 in the crust of Southern California at depths < 5 km. Thus, the high attenuation in the shallow crust obtained in this study may not be unique, but rather common. Because the depths of the events were > 4 km (Figs. S1 and S3), the depth variations in the Q_s values shallower than 4 km were not resolved well in our analysis. A value of approximately 55 at a depth of < 4 km represents the average value for layers in this depth range. The trend of very few earthquakes at depths < 4 km in this region (Figs. S1 and S3) may be related to the small Q-values at this depth.

Radiated energy (E_R) is an essential parameter for summarizing earthquake radiation processes and reflecting earthquake rupture dynamics. The combination of E_R with seismic moment (M_0), which represents the static size of an earthquake, aids in

655 understanding the physical processes of earthquakes of different magnitudes (Kanamori
656 & Heaton, 2000); moment-scaled radiated energy ($e_R = E_R/M_0$) allows comparison of
657 earthquakes with different sizes. Not only that, source parameters for small events may
658 be a rare source of information about processes in the seismogenic region (e.g., fluid
659 movement that may influence fault strength). Some previous studies showed that e_R
660 increases with M_w (e.g., Abercrombie 1995; Mayeda & Walter 1996; Izutani &
661 Kanamori 2001; Prejean & Ellsworth 2001; Mori et al. 2003; Takahashi et al. 2005;
662 Mayeda et al. 2005; Malagnini et al. 2014), while others suggested that the e_R is
663 independent of M_w (e.g., Ide & Beroza 2001; Pérez-Campos & Beroza 2001; Baltay et al.
664 2014; Zollo et al. 2014; Denolle & Shearer 2016; Ye et al. 2016; Chounet and Vallée,
665 2018). Many recent results show that e_R of M_w 2–5 events are not so different from
666 that of larger events (M_w > 6) (e.g., Ide & Beroza, 2001). Still, the estimation of E_R,
667 and hence e_R, includes an estimation error of a few times of magnitude even using
668 modern, high-quality data even for M_w > 6 events (Kanamori et al., 2020). It is still
669 important to investigate the scale dependence of e_R with greater accuracy and fewer
670 assumptions. Our results show that e_R of the M_w 2.0–4.5 event is approximately
671 constant regardless of M_w, with a similar median value of 3.6×10^{-5} to those estimated
672 for larger events (Kanamori et al., 2020).

673 Many studies have used the empirical Green's function (EGF), which is the
674 waveform of a nearby smaller earthquake (EGF event) (Mueller, 1985; Hough et al.,
675 1997), to account for the propagation effect. Previous studies have shown that this
676 empirical approach is often more effective at accounting for the propagation effect than
677 other approaches assuminge Q-structure and site effects (Ide et al., 2003). However,
678 there are practical difficulties with this empirical approach. The results tend to be
679 unstable owing to noise in EGFs and subtle differences in locations and focal
680 mechanisms between the target and EGF events. The available frequencies are narrowed
681 because of the source finiteness of EGF events. In addition, source parameters cannot
682 be estimated for events that do not have appropriate eGFs. These place some limitations
683 on the estimation of e_R, and an approach that does not rely on EGFs is desirable for
684 analyzing high-frequency waveforms.

The low Q_s-values in the shallow crust obtained in this study indicate the importance of correctly understanding shallow structures when estimating source parameters for small events. In general, the smaller the magnitude of the event, the more important the higher-frequency information becomes because information near and above the source corner frequency is crucial for the accurate estimation of radiated energy (e.g., Ross et al., 2018). Figure 11 shows the results for e_R if we assume the empirically derived Q-model (Fig. 2c). In this case, the median estimate of e_R becomes approximately 3.0×10^{-6} (Fig. 11a), an order of magnitude smaller than the value obtained for $M_w > 6$ events. The effect of neglecting the shallow attenuation was greater for smaller events (Fig. 11c). The validity of our Q-model (Fig. 9a and b) is also supported by the previous results showing that a typical e_R for M_w 2.0–4.5 events is not an order of magnitude smaller than that of larger events ($M_w > 6$) (e.g., Ide & Beroza, 2001). The large difference in the obtained results clearly shows the strong influence of the shallow low Q layer on the estimation of E_R of small events, even if high-quality near-source data are available.

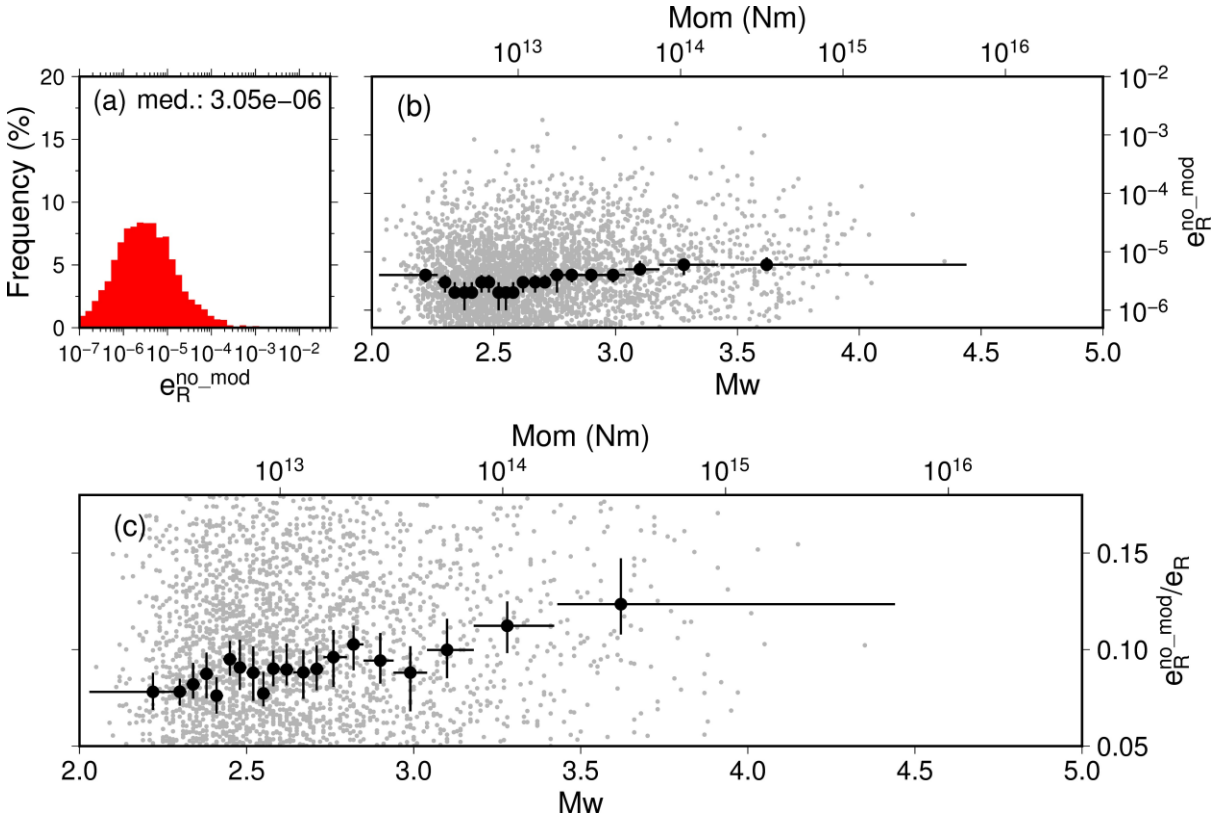

Figure. 11. Estimated scaled energy ($e_R^{\text{no\_mod}}$) without the modification of the Q-model. (a): Histograms of $e_R^{\text{no\_mod}}$. (b): $e_R^{\text{no\_mod}}$ compared with moment magnitude M_{w}. (c): $e_R^{\text{no}_{\text{mod}}}/e_R$ compared with moment magnitude M_{w}. Small gray circles represent individual results; large circles represent the median of each M_{w} range. The vertical line represents the 95% confidence range of the median value. The horizontal line represents the M_{w} range.

6. Conclusions

We detected high attenuation ($Q_s^{-1} = 55$) in the shallow (< 4 km) crust in the northern Ibaraki Prefecture, Japan, based on waveform modeling of high-quality near-source seismic data. Our estimates of the moment-scaled energies (e_R) based on the derived Q_s-model for 3,884 M_{w} 2.0–4.5 events vary around the median value of $e_R = 3.6 \times 10^{-5}$, which is similar to values reported for larger (M_{w} > 6) events. However, if we use an empirically derived Q_s-model (~350 at depths < 4 km), e_R erroneously becomes much smaller (median of 3.1×10^{-6}), requiring a significant increasing trend with M_{w}. Thus, the precise evaluation of the Q^{-1}-value in the shallow crust is crucial for the precise energy estimation of small events, even when high-quality near-source data are available. One possible reason for the low Q_s-value in this study may be that this region is seismically active. Faults, fracture zones, and fluids exist, and seismic waves may be attenuated as they pass through them. Alternatively, it may not be unusual for shallow Q_s-values to be extremely small, even for granite bodies.

Acknowledgments

The figures were created using GMT (Wessel & Smith, 2013). This study was financially supported by JSPS KAKENHI (grant number JP 20K14569).

Open Research

Data Availability Statement

This study used hypocenter and arrival time data from the JMA-Unified Catalog (https://www.data.jma.go.jp/svd/eqev/data/bulletin/hypo.html). Waveforms were obtained from the NIED Hi-net website (https://www.hinet.bosai.go.jp/?LANG=en). They were collected and stored by NIED Hi-net (2019). The figures were created using GMT (Wessel and Smith, 1998).

References

Abercrombie, R. E. (2000). Crustal attenuation and site effects at Parkfield, California. *Journal of Geophysical Research: Solid Earth*, *105*(B3), 6277–6286. https://doi.org/10.1029/1999jb900425

Abercrombie, R. E. (1995). Earthquake source scaling relationships from −1 to 5 ML using seismograms recorded at 2.5-km depth. *Journal of Geophysical Research: Solid Earth*, *100*(B12), 24015–24036. https://doi.org/10.1029/95jb02397

Abercrombie, R. E. (1997). Near-Surface Attenuation and Site Effects from Comparison of Surface and Deep Borehole Recordings. *Bulletin of the Seismological Society of America*.

Abercrombie, R. E., Trugman, D. T., Shearer, P. M., Chen, X., Zhang, J., Pennington, C. N., et al. (2021). Does Earthquake Stress Drop Increase With Depth in the Crust? *Journal of Geophysical Research: Solid Earth*, *126*(10). https://doi.org/10.1029/2021jb022314

Aki, K. (1967). Scaling law of seismic spectrum. *J Geophys Res 72, 1217–1231*.

Aki, K. (1980). Attenuation of shear-waves in the lithosphere for frequencies from 0.05 to 25 Hz. *Physics of the Earth and Planetary Interiors*, *21*(1), 50–60. https://doi.org/10.1016/0031-9201(80)90019-9

Anderson, J. G. (1986). Implication of Attenuation for Studies of the Earthquake Source. *Geophysical Monograph Series*, 311–318. https://doi.org/10.1029/gm037p0311

Anderson, J. G., & Hough, S. E. (1984). A model for the shape of the fourier amplitude spectrum of acceleration at high frequencies. *Bulletin of the Seismological Society of America*, *74*(5), 1969–1993. Retrieved from http://www.bssaonline.org/content/74/5/1969.short

Aster, R. C., & Shearer, P. M. (1991). High-frequency borehole seismograms recorded in the San Jcinto Fault zone, Southern California Part 2. Attenuation and site effects. *Bulletin of the Seismological Society of America*, *81*(4), 1081–1100. https://doi.org/10.1785/bssa0810041081

Baltay, A. S., & Hanks, T. C. (2014). Understanding the magnitude dependence of PGA and PGV in NGA-West 2 data. *Bulletin of the Seismological Society of America*, *104*(6), 2851–2865. https://doi.org/10.1785/0120130283

Brocher, T. M. (2008). Key elements of regional seismic velocity models for long period ground motion simulations. *Journal of Seismology*, *12*(2), 217–221. https://doi.org/10.1007/s10950-007-9061-3

Brune, J. (1970). Tectonic stress and the spectra of seismic shear waves from earthquakes. *Journal of Geophysical Research: Solid Earth*. Retrieved from http://onlinelibrary.wiley.com/doi/10.1029/JB075i026p04997/full

Chounet, A., & Vallée, M. (2018). Global and Interregion Characterization of Subduction Interface Earthquakes Derived From Source Time Functions Properties. *Journal of Geophysical Research: Solid Earth*, *123*(7), 5831–5852. https://doi.org/10.1029/2018jb015932

781 Dahm, T. (1996). Relative moment tensor inversion based on ray theory: Theory and
782 synthetic tests. *Geophysical Journal International*, *124*(1), 245–257.
783 https://doi.org/10.1111/j.1365-246X.1996.tb06368.x

784 Denolle, M. A., & Shearer, P. M. (2016). New perspectives on self-similarity for
785 shallow thrust earthquakes. *Journal of Geophysical Research: Solid Earth*, *121*(9),
786 6533–6565. https://doi.org/10.1002/2016jb013105

787 Eberhart-Phillips, D., Reyners, M., Chadwick, M., & Chiu, J.-M. (2005). Crustal
788 heterogeneity and subduction processes: 3-D Vp, Vp/Vs and Q in the southern
789 North Island, New Zealand. *Geophysical Journal International*, *162*(1), 270–288.
790 https://doi.org/10.1111/j.1365-246x.2005.02530.x

791 Edwards, B., & Rietbrock, A. (2009). A comparative study on attenuation and
792 source-scaling relations in the Kanto, Tokai, and Chubu regions of Japan, using
793 data from Hi-net and KiK-net. *Bulletin of the Seismological Society of America*,
794 *99*(4), 2435–2460. https://doi.org/10.1785/0120080292

795 Edwards, B., O. J. Ktenidou, F. Cotton, N. Abrahamson, C. Van Houtte, D. Fäh. (2015).
796 Epistemic uncertainty and limitations of the κ0 model for near-surface attenuation
797 at hard rock sites. *Geophys. J. Int. 202*, 1627–1645.
798 https://doi.org/10.1093/gji/ggv222

799 Eshelby, J. D. (1957). The determination of the elastic field of an ellipsoidal inclusion,
800 and related problems. *Proc Royal Soc Lond Ser Math Phys Sci, 241, 376–396.*

801 Eulenfeld, T., & Wegler, U. (2017). Crustal intrinsic and scattering attenuation of high-
802 frequency shear waves in the contiguous United States. *Journal of Geophysical*
803 *Research: Solid Earth*, *122*(6), 4676–4690. https://doi.org/10.1002/2017jb014038

804 Frankel, A. (1982). The effects of attenuation and site response on the spectra of
805 microearthquakes in the northeastern Caribbean. *Bulletin of the Seismological*
806 *Society of America, 72*(4), 1379–1402.

807 Fukushima, R., Nakahara, H., & Nishimura, T. (2016). Estimating S-Wave Attenuation
808 in Sediments by Deconvolution Analysis of KiK-net Borehole
809 SeismogramsEstimating S-Wave Attenuation in Sediments by Deconvolution
810 Analysis of KiK-net Borehole Seismograms. *Bulletin of the Seismological Society*
811 *of America, 106*(2), 552–559. https://doi.org/10.1785/0120150059

812 Haendel, A., Pilz, M., & Cotton, F. (2023). Hard-Rock κ0 at KiK-Net Sites in Japan.
813 *Bulletin of the Seismological Society of America*.
814 https://doi.org/10.1785/0120220246

815 Hanks, T. C. (1982). fmax. *Bulletin of the Seismological Society of America*.

816 Hasegawa, A., Umino, N., & Takagi, A. (1978). Double-planed structure of the deep
817 seismic zone in the northeastern Japan arc. *Tectonophysics, 47*(1–2), 43–58.
818 https://doi.org/10.1016/0040-1951(78)90150-6

819 Hassani, B., & Atkinson, G. M. (2018). Adjustable Generic Ground-Motion Prediction
820 Equation Based on Equivalent Point-Source Simulations: Accounting for Kappa
821 EffectsAdjustable Generic GMPE Based on Equivalent Point-Source Simulations.
822 *Bulletin of the Seismological Society of America, 108*(2), 913–928.
823 https://doi.org/10.1785/0120170333

824 Hauksson, E., & Shearer, P. M. (2006). Attenuation models (QP and QS) in three
825 dimensions of the southern California crust: Inferred fluid saturation at
826 seismogenic depths. *Journal of Geophysical Research: Solid Earth (1978–2012)*,
827 *111*(B5), n/a–n/a. https://doi.org/10.1029/2005jb003947

828 Hauksson, E., Teng, T., & Henyey, T. L. (1987). Results from a 1500 m deep,
829 three-level downhole seismometer array: Site response, low Q values, and fmax.
830 *Bulletin of the Seismological Society of America*, *77*(6), 1883–1904.
831 https://doi.org/10.1785/bssa0770061883

832 Hough, S. E. (1997). Empirical Green's function analysis: Taking the next step.
833 *Journal of Geophysical Research: Solid Earth*, *102*(B3), 5369–5384.
834 https://doi.org/10.1029/96jb03488

835 Hough, S. E. & Anderson, J. G. (1988). High-frequency spectra observed at Anza,
836 California: Implications for Q structure. *Bull. Seism. Soc. Am. 78*, 692–707.

837 Ide, S. (2003). Apparent break in earthquake scaling due to path and site effects on
838 deep borehole recordings. *Journal of Geophysical Research*, *108*(B5), 2271.
839 https://doi.org/10.1029/2001JB001617

840 Ide, S., & Beroza, G. C. (2001). Does apparent stress vary with earthquake size?
841 *Geophysical Research Letters*, *28*(17), 3349–3352.
842 https://doi.org/10.1029/2001GL013106

843 Izutani, Y., & Kanamori, H. (2001). Scale-dependence of seismic energy-to-moment
844 ratio for strike-slip earthquakes in Japan. *Geophysical Research Letters*, *28*(20),
845 4007–4010. https://doi.org/10.1029/2001GL013402

846 Kagan, Y. Y. (1991). 3-D rotation of double-couple earthquake sources. *Geophysical*
847 *Journal International*, *106*(3), 709–716.
848 https://doi.org/10.1111/j.1365-246X.1991.tb06343.x

849 Kanamori, H. & Heaton, T. H. (2000). Microscopic and Macroscopic Physics of
850 Earthquakes. *in GeoComplexity and the Physics of Earthquakes, Geophysical*
851 *Monograph Series, 120.*

852 Kanamori, H., Mori, J., Hauksson, E., Heaton, T. H., Hutton, L. K., & Jones, L. M.
853 (1993). Determination of earthquake energy release and ML using TERRAscope.
854 *Bulletin of the Seismological Society of America*, *83*(2), 330–346.

855 Kanamori, H., Ross, Z. E., & Rivera, L. (2020). Estimation of radiated energy using the
856 KiK-net downhole records - Old method for modern data. *Geophysical Journal*
857 *International*, *221*(2), 1029–1042. https://doi.org/10.1093/gji/ggaa040

858 Kato, A., Igarashi, T., Obara, K., Sakai, S., Takeda, T., Saiga, A., et al. (2013).
859 Imaging the source regions of normal faulting sequences induced by the 2011 M9.0
860 Tohoku-Oki earthquake. *Geophysical Research Letters*, *40*(2), 273–278.
861 https://doi.org/10.1002/grl.50104

862 Kato, A., Sakai, S., & Obara, K. (2011). A normal-faulting seismic sequence triggered
863 by the 2011 off the Pacific coast of Tohoku Earthquake: Wholesale stress regime
864 changes in the upper plate. *Earth, Planets and Space*, *63*(7), 745–748.
865 https://doi.org/10.5047/eps.2011.06.014

866 Kinoshita, S. (1994). Frequency-dependent attenuation of shear waves in the crust of
867 the southern Kanto area, Japan. *Bulletin of the Seismological Society of America*,
868 *84*(5), 1387–1396. https://doi.org/10.1785/bssa0840051387

869 Kinoshita, S., & Ohike, M. (2002). Scaling Relations of Earthquakes That Occurred in
870 the Upper Part of the Philippine Sea Plate beneath the Kanto Region, Japan,
871 Estimated by Means of Borehole Recordings. *Bulletin of the Seismological Society*
872 *of America*, *92*(2), 611–624. https://doi.org/10.1785/0120010134

873 Kissling, E., Ellsworth, W. L., Eberhart-Phillips, D., & Kradolfer, U. (1994). Initial
874 reference models in local earthquake tomography. *Journal of Geophysical*
875 *Research: Solid Earth*, *99*(B10), 19635–19646. https://doi.org/10.1029/93jb03138

876 Kubo, A., Fukuyama, E., Kawai, H., & Nonomura, K. (2002). NIED seismic moment
877 tensor catalogue for regional earthquakes around Japan: quality test and
878 application. *Tectonophysics*, *356*(1–3), 23–48.
879 https://doi.org/10.1016/S0040-1951(02)00375-X

880 Lin, Y., & Jordan, T. H. (2018). Frequency-Dependent Attenuation of P and S Waves in
881 Southern California. *Journal of Geophysical Research: Solid Earth*, *123*(7), 5814–
882 5830. https://doi.org/10.1029/2018jb015448

883 Ludwig, W. J., Nafe, J. E., & Drake, C. L. (1970). Seismic refraction, The Sea, 4 (1),
884 53–84. *VViley-Intersci., NY*.

885 Malagnini, L., Irene Munafo', Massimo Cocco, Stefan Nielsen, Kevin Mayeda, and
886 Enzo Boschi (2014). Gradual Fault Weakening with Seismic Slip: Inferences from
887 the Seismic Sequences of L'Aquila, 2009, and Northridge, 1994. *Pure Appl*
888 *Geophys 171, 2709–2730.* https://doi.org/10.1007/s00024-013-0752-0.

889 Mayeda, K. & Walter, W. R. (1996). Moment, energy, stress drop, and source spectra of
890 western United States earthquakes from regional coda envelopes. *J Geophys Res*
891 *Solid Earth 101, 11195–11208.* https://doi.org/10.1029/96JB00112.

892 Mayeda, K., Gök, R., Walter, W. R. & Hofstetter. (2005). A. Evidence for non-constant
893 energy/moment scaling from coda-derived source spectra. *Geophys Res Lett, 32*
894 *(10).* https://doi.org/10.1029/2005GL022405

895 Mori, J., Abercrombie, R. E. & Kanamori, H. (2003). Stress drops and radiated energies
896 of aftershocks of the 1994 Northridge, California, earthquake. *J Geophys Res Solid*
897 *Earth, 108*, 1978-2012. https://doi.org/10.1029/2001JB000474.

898 Moya, A., & Irikura, K. (2003). Estimation of Site Effects and Q Factor Using a
899 Reference Event. *Bulletin of the Seismological Society of America*, *93*(4), 1730–
900 1745. https://doi.org/10.1785/0120020220

Mueller, C. S. (1985). Source pulse enhancement by deconvolution of an empirical Green's function. *Geophysical Research Letters*, *12*(1), 33–36. https://doi.org/10.1029/gl012i001p00033

Nakajima, J., & Matsuzawa, T. (2017). Anelastic properties beneath the Niigata--Kobe tectonic zone, Japan. *Earth, Planets and Space*, *69*(1), 1–9.

Nakamura, R., & Shiina, T. (2019). Three-dimensional S-wave attenuation structure in and around source area of the 2018 Hokkaido Eastern Iburi Earthquake, Japan. *Earth, Planets and Space*, *71*(1), 114. https://doi.org/10.1186/s40623-019-1095-6

NIED. (2019). NIED Hi-net, National Research Institute for Earth Science and Disaster Resilience. https://doi.org/10.17598/NIED.0003

Oth, A., Bindi, D., Parolai, S., & Di Giacomo, D. (2010). Earthquake scaling characteristics and the scale-(in)dependence of seismic energy-to-moment ratio: Insights from KiK-net data in Japan. *Geophysical Research Letters*, *37*(19), https://doi.org/10.1029/2010GL044572

Oth, A., Bindi, D., Parolai, S. & Giacomo, D. D. (2011). Spectral Analysis of K-NET and KiK-net Data in Japan, Part II: On Attenuation Characteristics, Source Spectra, and Site Response of Borehole and Surface StationsSpectral Analysis of K-NET and KiK-net Data in Japan, Part II. *Bulletin of the Seismological Society of America*, *101*, 667–687.

Pennington, C. N., Wu, Q., Chen, X., & Abercrombie, R. E. (2023). Quantifying rupture characteristics of microearthquakes in the Parkfield Area using a high-resolution borehole network. *Geophysical Journal International*, *233*(3), 1772–1785. https://doi.org/10.1093/gji/ggad023

Prudencio, J., Manga, M., & Taira, T. (2018). Subsurface Structure of Long Valley Caldera Imaged With Seismic Scattering and Intrinsic Attenuation. *Journal of*

926 *Geophysical Research: Solid Earth*, *123*(7), 5987–5999.
927 https://doi.org/10.1029/2017jb014986

928 Qiu, H., Ben-Zion, Y., Ross, Z. E., Share, P.-E., & Vernon, F. L. (2017). Internal
929 structure of the San Jacinto fault zone at Jackass Flat from data recorded by a
930 dense linear array. *Geophysical Journal International*, *209*(3), 1369–1388.
931 https://doi.org/10.1093/gji/ggx096

932 Ross, Z. E., Kanamori, H., Hauksson, E., & Aso, N. (2018). Dissipative Intraplate
933 Faulting During the 2016 Mw 6.2 Tottori, Japan Earthquake. *Journal of*
934 *Geophysical Research: Solid Earth*, *123*(2), 1631–1642.
935 https://doi.org/10.1002/2017JB015077

936 Sato, H., Fehler, M., & Maeda, T. (2012). *Seismic Wave Propagation and Scattering in*
937 *the Heterogeneous Earth* (2nd ed.). Springer Berlin Heidelberg.
938 https://doi.org/10.1007/978-3-642-23029-5

939 Snoke, J. A. (1987). STABLE DETERMINATION OF (BRUNE) STRESS DROPS.
940 *Bulletin of the Seismological Society of America*, *77(2)*, 530-538.

941 Takahashi, T., Sato, H., Ohtake, M., & Obara, K. (2005). Scale Dependence of
942 Apparent Stress for Earthquakes along the Subducting Pacific Plate in
943 Northeastern Honshu, Japan. *Bulletin of the Seismological Society of America*,
944 *95*(4), 1334–1345. https://doi.org/10.1785/0120040075

945 Takemura, S., Furumura, T., & Saito, T. (2009). Distortion of the apparent S-wave
946 radiation pattern in the high-frequency wavefield: Tottori-Ken Seibu, Japan,
947 earthquake of 2000. *Geophysical Journal International*, *178*(2), 950–961.
948 https://doi.org/10.1111/j.1365-246x.2009.04210.x

949 Trugman, D. T., Chu, S. X., & Tsai, V. C. (2021). Earthquake Source Complexity
950 Controls the Frequency Dependence of Near-Source Radiation Patterns.
951 *Geophysical Research Letters*, *48*(17). https://doi.org/10.1029/2021gl095022

952 Uchide, T., & Imanishi, K. (2016). Small Earthquakes Deviate from the Omega-Square
953 Model as Revealed by Multiple Spectral Ratio AnalysisShort Note. *Bulletin of the*
954 *Seismological Society of America*, (3). https://doi.org/10.1785/0120150322

955 Ueno, H., Hatakeyama, S., Aketagawa, T., Funasaki, J., & Hamada, N. (2002).
956 Improvement of hypocenter determination procedures in the japan meteorological
957 agency. *Q. J. Seism*, *65*, 123–134.

958 Umeda, K. (2015). Localized extensional tectonics in an overall reverse-faulting
959 regime, Northeast Japan. *Geoscience Letters*, *2*(1), 1–8.

960 Yuta Usuda, Takashi Iidaka, Eiji Kurashimo, Toshihiro Igarashi, Kazushige Obara,
961 Aitaro Kato, et al. (2022). Imaging of S Wave Reflection Boundaries in the Crust
962 Obtained from a Dense Seismic Array at the Northern Part of Ibaraki and Iwaki
963 Area. *Zisin 2*, *75*(0), 125–143. https://doi.org/10.4294/zisin.2021-13

964 Vassiliou, M. S., & Kanamori, H. (1982). The energy release in earthquakes. *Bulletin of*
965 *the Seismological Society of America*, *72*(2), 371–387.

966 Venkataraman, A., & Kanamori, H. (2004). Observational constraints on the fracture
967 energy of subduction zone earthquakes. *Journal of Geophysical Research: Solid*
968 *Earth*, *109*(5). https://doi.org/10.1029/2003JB002549

969 Wang, Q.-Y., Frank, W. B., Abercrombie, R. E., Obara, K., & Kato, A. (2023). What
970 makes low-frequency earthquakes low frequency. *Science Advances*, *9*(32),
971 eadh3688. https://doi.org/10.1126/sciadv.adh3688

Wessel, P., Smith, W. H. F., Scharroo, R., Luis, J., & Wobbe, F. (2013). Generic mapping tools: improved version released. *Eos, Transactions American Geophysical Union*, *94*(45), 409–410.

Yamaya, L., Mochizuki, K., Akuhara, T., Takemura, S., Shinohara, M., & Yamada, T. (2022). CMT inversion for small-to-moderate earthquakes applying to dense short-period OBS array at off Ibaraki region. *Earth, Planets and Space*, *74*(1), 164. https://doi.org/10.1186/s40623-022-01721-3

Ye, L., Lay, T., Kanamori, H., & Rivera, L. (2016). Rupture characteristics of major and great (Mw ≥ 7.0) megathrust earthquakes from 1990 to 2015: 1. Source parameter scaling relationships. *Journal of Geophysical Research: Solid Earth*, *121*(2), 826–844. https://doi.org/10.1002/2015JB012426

Yoshida, K. (2019). Prevalence of asymmetrical rupture in small earthquakes and its effect on the estimation of stress drop: a systematic investigation in inland Japan. Geoscience Letters, 6(1). https://doi.org/10.1186/s40562-019-0145-z

Yoshida, K. (2023). Direct Evidence for Diverse Source Complexity in Small Earthquakes (Mw3.3-5.0) Obtained from Short-Range Borehole Seismic Data. *ESS Open Archive*, https://doi.org/10.22541/essoar.170224459.93746071/v1.

Yoshida, K. (2021). Detection of temporal change in near-source attenuation during intense fluid-driven seismicity following the 2011 Tohoku-Oki earthquake. *Geophys J Int*, 224, 138–150, https://doi.org/10.1093/gji/ggaa421

Yoshida, K., & Kanamori, H. (2023). Time-domain source parameter estimation of Mw 3–7 earthquakes in Japan from a large database of moment-rate functions. *Geophysical Journal International, 234, 243–262*. https://doi.org/10.1093/gji/ggad068

Yoshida, K., Hasegawa, A., & Okada, T. (2015). Spatially heterogeneous stress field in the source area of the 2011 Mw6.6 Fukushima-Hamadori earthquake, NE Japan, probably caused by static stress change. *Geophysical Journal International*, *201*(2), 1062–1071. https://doi.org/10.1093/gji/ggv068

Yoshida, K., Hasegawa, A., Yoshida, T., & Matsuzawa, T. (2019a). Heterogeneities in Stress and Strength in Tohoku and Its Relationship with Earthquake Sequences Triggered by the 2011 M9 Tohoku-Oki Earthquake. *Pure and Applied Geophysics*, *176*(3), 1335–1355. https://doi.org/10.1007/s00024-018-2073-9

Yoshida, K., Saito, T., Emoto, K., Urata, Y., & Sato, D. (2019b). Rupture directivity, stress drop, and hypocenter migration of small earthquakes in the Yamagata-Fukushima border swarm triggered by upward pore-pressure migration after the 2011 Tohoku-Oki earthquake. *Tectonophysics*, *769*. https://doi.org/10.1016/j.tecto.2019.228184

Yoshimoto, K., Sato, H., Iio, Y., Ito, H., Ohminato, T., & Ohtake, M. (1998). Frequency-dependent Attenuation of High-frequency P and S Waves in the Upper Crust in Western Nagano, Japan. *Pure and Applied Geophysics*, *153*(2), 489–502. https://doi.org/10.1007/s000240050205

Yoshida, K., Saito, T., Urata, Y., Asano, Y., & Hasegawa, A. (2017). Temporal Changes in Stress Drop, Frictional Strength, and Earthquake Size Distribution in the 2011 Yamagata-Fukushima, NE Japan, Earthquake Swarm, Caused by Fluid Migration. *Journal of Geophysical Research: Solid Earth*, *122*(12), 10,379-10,397. https://doi.org/10.1002/2017JB014334

Zhao, D., Kitagawa, H., & Toyokuni, G. (2015). A water wall in the Tohoku forearc causing large crustal earthquakes. *Geophysical Journal International*, *200*(1), 149–172. https://doi.org/10.1093/gji/ggu381

1021 Zhu, L., & Rivera, L. (2002). A note on the dynamic and static displacements from a
1022 point source in multilayered media. *Geophysical Journal International*, *148*(3),
1023 619–627. https://doi.org/10.1046/j.1365-246X.2002.01610.x

1024 Zollo, A., Orefice, A. & Convertito, V. (2014). Source parameter scaling and radiation
1025 efficiency of microearthquakes along the Irpinia fault zone in southern Apennines,
1026 Italy. *J Geophys Res Solid Earth*, *119*, 3256–3275,
1027 https://doi.org/10.1002/2013JB010116.

1028

1029

1030

1031

1032

Figure 1.

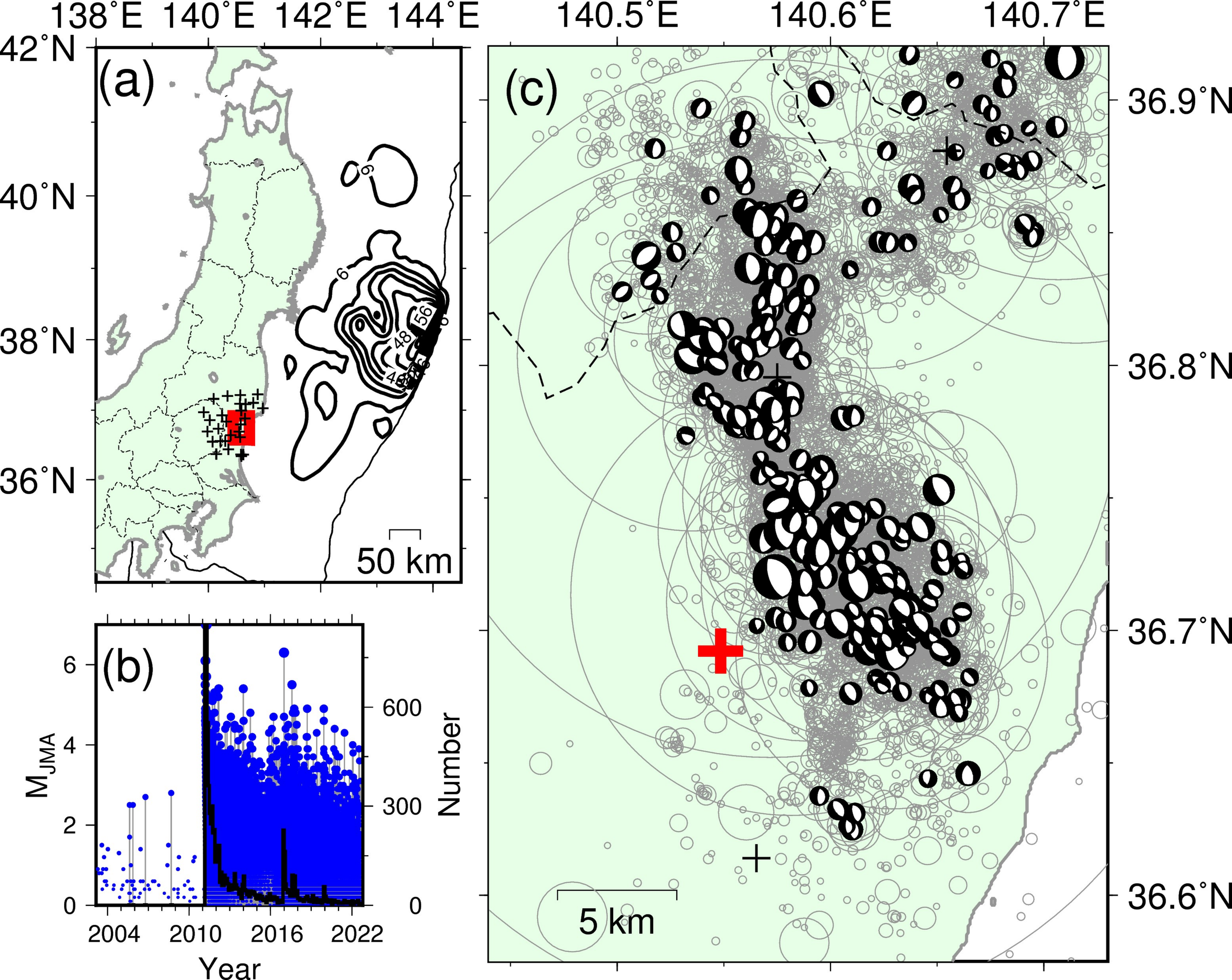
138°E
140°E
142°E
144°E
42°N
40°N
38°N
36°N
(a)
6
6
48
56
50 km
(b)
6
4
2
0
M_{JMA}
600
300
0
Number
2004
2010
2016
2022
Year
140.5°E
140.6°E
140.7°E
36.9°N
36.8°N
36.7°N
36.6°N
(c)
5 km

Figure 2.

(a)

140.5°
140.6°
140.7°
36.9°
36.8°
36.7°
36.6°
A
A'
B
B'
C
C'
D
D'
E
E'
F
F'
G
G'
H
H'
I
I'
5.0 km
4
6
8
10
Depth (km)

(b)

0
2
4
6
8
Velocity (km/s)

(c)

0
400
800
Q

(d)

2.5
3.0
Density (kg/cm^3)

0
5
10
15
20
25
Depth (km)

Figure 3.

(a) F–net M_w<4.0

(b) M_{JMA}: 2.0–4.0

(c) M_{JMA}: 1.0–2.0

140.5˚ 140.6˚ 140.7˚

36.9˚ 36.8˚ 36.7˚ 36.6˚

(d) n=217

(e) n=7952

(f) n=23811

Frequency (%)

30.0 20.0 10.0 0.0

1.5 2.0 2.5 3.0 3.5 4.0

Mw

Figure 4.

(a) N.JUOH, 20110924211107 29 (M_w1.8), del=5.7 km, z=4.6 km, az=242 °, t_p=1.30s

U (obs)

R (obs)

T (obs)

U (syn)

R (syn)

T (syn)

0.8
0.4
0.0
−0.4
−0.8

0.0 0.5 1.0 1.5 2.0 2.5

Time from P onset (s)

(b)

(c)

(d)

Δt_p^*= 0.00844

Δt_s^*= 0.02417

Amp. (PU)

Amp. (SU)

Res. (O–C)

10^{-2} 10^{-3} 10^{-4} 10^{-5} 10^{-6} 10^{-7} 10^{-8}

10^{3} 10^{2} 10^{1} 10^{0} 10^{-1} 10^{-2} 10^{-3}

10.0 20.0 30.0

Frequency (Hz)

Figure 5.

(a) med.: 0.01231 (0.01168 – 0.01279)

Number

Δts^*

(b)

Δts^*

Epicentral Distance (km)

(c) med.: 0.00230 (0.00194 – 0.00281)

Number

Δtp^*

(d)

Δtp^*

Epicentral Distance (km)

Figure 6.

(a)

med.: 0.00391 (0.00381 – 0.00414)

Number

100
80
60
40
20
0

–0.02
0.00
0.02

Δq_s^{-1}

(b)

Δq_s^{-1}

0.02
0.01
0.00
–0.01

0.00
3.00
6.00
9.00
12.00

Epicentral Distance (km)

(c)

med.: 0.00130 (0.00105 – 0.00154)

Number

100
80
60
40
20
0

–0.02
0.00
0.02

Δq_p^{-1}

(d)

Δq_p^{-1*}

0.02
0.01
0.00
–0.01

0.00
3.00
6.00
9.00
12.00

Epicentral Distance (km)

Figure 7.

S–wave

P–wave

(a) 17–20 Hz

(b) 17–20 Hz

(c) 17–20 Hz

(d) 17–20 Hz

(e) 14–17 Hz

(f) 14–17 Hz

(g) 14–17 Hz

(h) 14–17 Hz

(i) 11–14 Hz

(j) 11–14 Hz

(k) 11–14 Hz

(l) 11–14 Hz

(m) 8–11 Hz

(n) 8–11 Hz

(o) 8–11 Hz

(p) 8–11 Hz

(q) 5–8 Hz

(r) 5–8 Hz

(s) 5–8 Hz

(t) 5–8 Hz

$r_{i5} = \ln R(f_5)$

$r_{i4} = \ln R(f_4)$

$r_{i3} = \ln R(f_3)$

$r_{i2} = \ln R(f_2)$

$r_{i1} = \ln R(f_1)$

2

0

−2

0 3 6 9 12

Del (km)

Del. (km)

Figure 8.

(a)

Q_s

0 300 600 900

(b)

Q_p

0 300 600 900

Depth (km)

0 2 4 6 8 10 12 14 16 18 20

Figure 9.

(a) med.: 3.64e–05

Frequency (%)

10^{-7} 10^{-6} 10^{-5} 10^{-4} 10^{-3} 10^{-2}

$e_R=E_R/M_0$

(b)

Mom (Nm)

10^{13} 10^{14} 10^{15} 10^{16}

e_R

Mw

(c)

e_R

Depth (km)

Figure 10.

(a) Refined Q–model

Q_s = 400

Q_s = 55

Ar (m^2)

10^4 10^3 10^2 10^1 10^0 10^{-1}

0.0 10.0 20.0 30.0

(b) Original Q–model

Q_s = 400

Q_s = 55

Ar (m^2)

10^5 10^4 10^3 10^2 10^1 10^0

0.0 10.0 20.0 30.0

Travel Time (s)

Figure 11.

(a) med.: 3.05e−06

Frequency (%)

$e_R^{no\_mod}$

(b)

Mom (Nm)

Mw

$e_R^{no\_mod}$

(c)

Mom (Nm)

Mw

$e_R^{no\_mod}/e_R$